

Polariton-polariton coherent coupling in a molecular spin-superconductor chip

Carolina del Río,¹ Marcos Rubín-Osanz,¹ David Rodríguez,² Sebastián Roca-Jerat,¹ María Carmen Pallarés,^{1,3} J. Alejandro de Sousa,⁴ Paweł Pakulski,⁵ José Luis García Palacios,¹ Daniel Granados,⁶ Dawid Pinkowicz,⁵ Núria Crivillers,⁴ Anabel Lostao,^{1,3,7} David Zueco,¹ Alicia Gomez,² and Fernando Luis¹

¹*Instituto de Nanociencia y Materiales de Aragón (INMA),
CSIC-Universidad de Zaragoza, 50009, Zaragoza, Spain*

²*Centro de Astrobiología (CAB), CSIC-INTA, 28850 Torrejón de Ardoz, Madrid, Spain*

³*Laboratorio de Microscopias Avanzadas (LMA),
Universidad de Zaragoza, 50018 Zaragoza, Spain*

⁴*Instituto de Ciencia de Materiales de Barcelona (ICMAB), CSIC, Barcelona, Spain*

⁵*Jagiellonian University, Faculty of Chemistry, Krakow, Poland*

⁶*IMDEA-Nanoscience, Cantoblanco, 28049 Madrid, Spain*

⁷*Fundación ARAID, 50018 Zaragoza, Spain*

The ability to establish coherent communication channels is key for scaling up quantum devices. Here, we engineer interactions between distant polaritons, hybrid spin-photon excitations formed at different lumped-element superconducting resonators within a chip. The chip consists of several resonator pairs, slightly detuned in frequency to make them addressable, capacitively coupled within each pair and inductively coupled to a common readout line. They interact locally with samples of PTMr and Tripak⁻ organic free radicals, deposited onto their inductors, which provide model $S = 1/2$, $g \simeq 2$ spin ensembles. Frequency-dependent microwave transmission experiments, performed at very low temperatures, measure polariton frequencies as a function of magnetic field in different scenarios. When only one resonator within a pair hosts a molecular sample, the results evidence that spins couple remotely to the empty LER as well as to the local cavity mode. If both resonators interact with a spin ensemble, the magnetic field tunes the polariton frequencies relative to each other, on account of the different spin-photon interactions at each LER. When polaritons are brought into mutual resonance, an avoided level crossing emerges that gives direct spectroscopic evidence for a coherent polariton-polariton interaction mediated by the circuit. Pump-probe experiments reveal that the excitation of a polariton within a connected pair is felt, thus it can be read out, by the other one. These observations, backed by model calculations, illustrate the control and detection of distant photon-photon and spin-spin correlations and entanglement in a scalable modular chip.

I. INTRODUCTION

Circuit quantum electrodynamics (circuit QED) studies quantum matter interacting with photon modes of superconducting cavities [1, 2]. Besides the fundamental interest of accessing strong [3] and ultra-strong [4] light-matter interaction regimes, circuit QED provides also a platform for reading out solid-state qubits [5], for generating quantum states of light [6] and for quantum sensing [7], among others. In addition, photons introduce effective interactions between qubits coupled to the same cavity, which can be exploited for establishing coherent communication channels and, therefore, scaling up quantum computing architectures. Such a quantum bus has been realized with superconducting qubits [8] and with spin qubits in semiconductors [9–11], both of which couple to the electric photon field.

The magnetic spin-photon interaction is much weaker, but it is enhanced in the case of macroscopic spin ensembles [12–21]. This has allowed coupling collective excitations of two distant samples, either organic free radicals [22] or NV⁻ centers in diamond crystals [23], through a coplanar superconducting resonator. The need of coupling both ensembles to the same cavity mode adds, however, some constraints. For instance, they must be located at specific positions determined by the photon magnetic

field profile. Besides, one of the resulting coupled states is always dark, which precludes a direct determination of the circuit mediated interaction by spectroscopic measurements.

In this work, we move beyond these limitations and explore a modular hybrid quantum platform, in which distant polaritons, i.e. light-matter hybrid states generated by local spin-photon interactions at different lumped-element superconducting cavities, can be tuned by a magnetic field, addressed in situ in a multiplexable manner and coherently coupled. This scheme offers the possibility of generating, tuning and detecting excitations that simultaneously involve spin *and* photon entanglement. It has also a high design flexibility, e.g. to build in asymmetries that turn each polariton distinguishable from the others, and it is inherently scalable to multiple nodes, which would make it relevant for applications to quantum simulation [24, 25] and quantum computing [26, 27].

II. EXPERIMENTAL SETUP

A. Superconducting circuits

The device used in this work is sketched in Figs. 1a and 1b, and described in detail in Appendix A 1. The chip

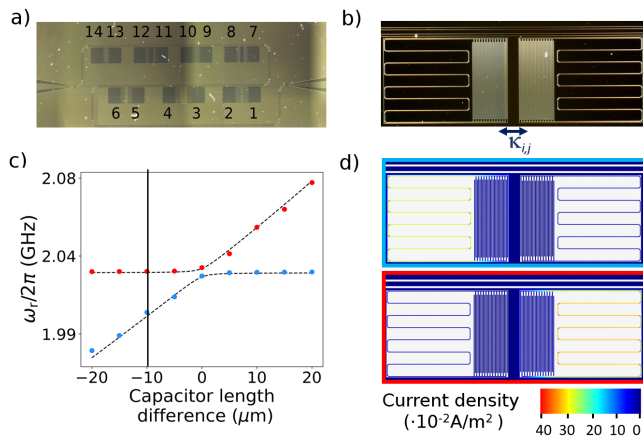


FIG. 1: a) Image of a chip hosting seven superconducting lumped element resonator (LER) pairs coupled to a common transmission line. b) Optical microscopy image of one of these capacitively coupled LER pairs. c) Resonance frequencies of a LER pair calculated as a function of the difference between their finger capacitor lengths. The coupling introduces a mode splitting $\Delta\omega_r = 2\kappa_{i,j}$ when the two LERs become identical. d) Single-photon current density simulations for the two resonant modes of a detuned LER pair (vertical line in panel c). Further details on the design, simulation, fabrication and characterization of the chips are given in Appendices A 1 and A 4.

consists of 7 pairs of superconducting lumped-element LC resonators (LERs), all coupled to the same readout line [21, 28]. They are fabricated by maskless optical lithography on a 125 nm thick NbTiN film deposited by sputtering onto a silicon wafer. The relevant properties of each superconducting LER, i.e., its resonance frequency $\omega_{r,i}$ and the photon loss rate κ_i ($i = 1, \dots, 14$), can be tailored within a wide range without affecting the transmission properties of the device. In the chip of Fig. 1a, different $\omega_{r,i}/2\pi$ ranging from 1.7 GHz to 3.3 GHz were tuned by varying the capacitor geometries while leaving all inductors, which provide the coupling to the spin samples, the same. This allows multiplexing the LER readout, as shown in Appendices A 1 and A 4. The two LERs within each pair are capacitively coupled, with a coupling strength $\kappa_{i,j}$ that is controlled by the separation between their respective capacitors. If they were identical, this coupling would lead to an avoided level crossing, shown in Fig. 1c, with a frequency splitting $\Delta\omega_r = 2\kappa_{i,j}$ [29] between symmetric and anti-symmetric modes delocalized all over the LER pair (Fig. 7 from Appendix A 1). Here, we detune the ‘bare’ resonance frequencies $\omega_{r,i}$ and $\omega_{r,j}$ of the two LERs by making the lengths of their interdigitated capacitors different. When $|\omega_{r,i} - \omega_{r,j}| > \kappa_{i,j}$, the photon magnetic field becomes predominantly localized at either one or the other LER (Fig. 1d and Fig. 7). This sort of ‘dispersive’ condition ensures that, in spite of their mutual coupling, each of them can still be addressed

by choosing the appropriate frequency.

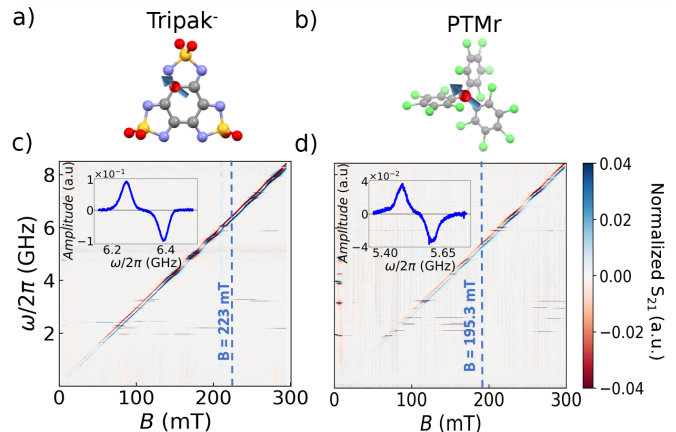


FIG. 2: Molecular structures of the organic free radical molecules used in this study: a) Tripak⁻ [30]; b) PTMr [31]. Here, carbon atoms are represented in grey, chlorine atoms in green, nitrogen atoms in blue, sulfur atoms in yellow and oxygen atoms in red. c) and d) Broadband microwave absorption spectra of Tripak⁻ and PTMr, respectively, measured at $T = 11 \text{ mK}$ by coupling them to a superconducting transmission line. The insets show normalized transmission data measured at the magnetic fields indicated by vertical dashed lines.

B. Synthesis, characterization and integration of model spin ensembles

These LERs host samples of two different organic free-radical molecules. The molecular structures of perchlorotriphenylmethyl (PTMr) and benzo[1,2-c:3,4-c':5,6-c'']tris([1,2,5]thiadiazole)2,2,5,5,8,8-hexaoxide (Tripak⁻) radicals, synthesized by following chemical procedures reported elsewhere [30–32], are shown in Figs. 2a and 2b. These molecules were transferred from solution onto the LER inductors and then left dry in the dark (see Appendix A 2 for details). The solution contained also a polystyrene polymer that prevents agglomeration of the radical molecules in the dry deposits. Each of these deposits is then highly stable at ambient conditions and provides a model ensemble of $N \sim 5 \times 10^{12} - 5 \times 10^{14}$ identical $S = 1/2$ spins with a quasi-isotropic g factor, very close to that of a single electron. The latter property leads, at any magnetic field B and despite the random molecular orientations, to a well-defined narrow spin resonance, which was characterized as a function of B by coupling these spin samples to a superconducting waveguide. Representative results, measured at very low temperatures and normalized as described in [33, 34], are shown in Figs. 2c and 2d. Additional data are shown in Fig. 9 from Appendix A 2. The spin resonance frequency Ω_S increases linearly with B , as expected for a paramagnetic system. The slightly

different slopes reveal different g factors, 2.001 for PTMr and 2.003 for Tri^{p^-} . The resonance line shape, shown in the insets of Fig. 2, allows estimating the spin line width $\gamma/2\pi \simeq 7 - 12$ MHz for both samples, depending on concentration.

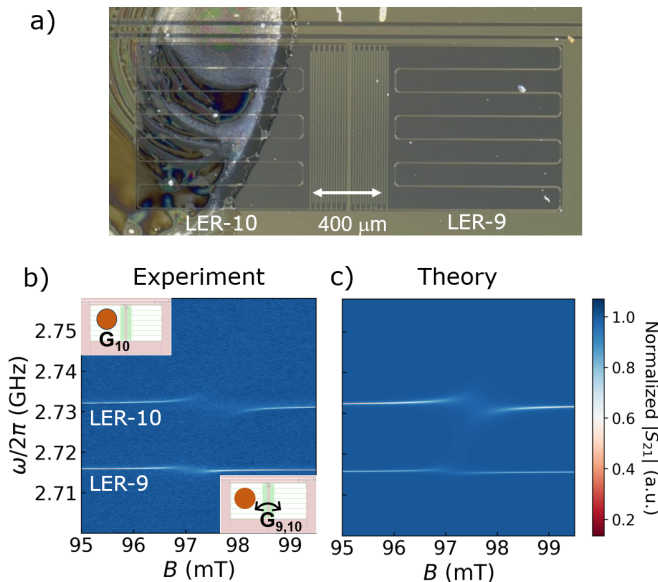


FIG. 3: a) Optical microscopy image of a $N \sim 5 \times 10^{12}$ PTMr free radical deposit on the inductor of LER-10, forming a coupled pair with LER-9, which remains empty. b) Colour plot of the microwave transmission amplitude $|S_{21}|$ measured, at $T = 11$ mK, near the resonance frequencies of the two LERs. The data show a detectable coupling of the spins to both resonant modes, being $G_{10}/2\pi = 5.4$ MHz the coupling strength to the ‘local’ LER-10 and $G_{9,10}/2\pi = 2.5$ MHz the remote interaction with LER-9. c) Theoretical calculation of the microwave transmission obtained from Eq. (1) by using input-output theory (Appendices D 2 and D 3), for $G_{10}/2\pi = 5.4$ MHz and $\kappa_{9,10}/2\pi = 6.5$ MHz.

III. RESULTS

A. One spin ensemble coupled to a LER pair: remote spin photon coupling

Let’s now move into the response of LER-spin units. We first consider the situation, shown in Fig. 3a, in which only one of the LERs, LER-10, hosts a sample of $N \sim 5 \times 10^{12}$ PTMr molecules, while the second one, LER-9, remains empty. With this setup, we aim to compare the couplings of the same spin ensemble to local and remote photon modes. Microwave transmission data S_{21} were measured at very low temperature as a function of frequency and magnetic field using the setup described in Appendices A 3 and A 4. Results are shown in Fig. 3b. The two modes appear as horizontal lines at slightly dif-

ferent frequencies. When the magnetic field brings the spins to resonance with LER-10, the transmission shows a frequency shift, a broadening and a reduced visibility of this mode, which characterize the local spin-photon coupling. Fitting these data using input-output theory (described in Appendices D 2 and D 3) gives a collective spin-photon coupling strength $G_{10}/2\pi = 5.4$ MHz, which corresponds to high cooperativity $C \equiv G_{10}^2/\kappa\gamma \sim 70$. Interestingly, the same spin ensemble also couples to the photon mode of the nominally empty resonator LER-9. The remote coupling rate $G_{9,10}/2\pi \simeq 2.5$ MHz, is only two times smaller than the local G_{10} . Hybrid excitations generated at LER-10 are therefore detected by measuring the response of LER-9.

These data can be understood within the framework of the ‘two-resonator’ circuit QED theory [35], which generalizes the usual Jaynes-Cummings formalism to the case of multiple cavities. The Hamiltonian describing the hybrid system can be written as follows

$$\mathcal{H} = \sum_{q=i,j} (\omega_{r,q} a_q^\dagger a_q + \Omega_{S,q} S_q^z) + \sum_{q=i,j} G_q (a_q S_q^+ + a_q^\dagger S_q^-) + \kappa_{i,j} (a_i^\dagger a_j + a_i a_j^\dagger), \quad (1)$$

where a_q and a_q^\dagger represent the photon annihilation and creation, respectively, operators in each cavity $q = i, j$, and S_q^α with $\alpha = \{z, +, -\}$ represent the conventional spin-1/2 operators. For the system of Fig. 3, $i = 9$ and $j = 10$, and only G_{10} and Ω_{10} are nonzero since LER-9 is empty. Solving for the eigenvalues and eigenstates of (1), as detailed in Appendix D 1 a, shows that the remote $G_{9,10}$ is a direct manifestation of the interactions brought about by the circuit and gives the relation

$$G_{9,10} = \frac{G_{10}}{\sqrt{2}} \sqrt{1 - \frac{|\omega_{r,9} - \omega_{r,10}|}{\sqrt{|\omega_{r,9} - \omega_{r,10}|^2 + 4\kappa_{9,10}^2}}}. \quad (2)$$

Equation (2) allows estimating $\kappa_{9,10} = 6.5$ MHz, which is reasonably close to the value $\kappa_{9,10} = 5.8$ MHz derived from the circuit simulation (Appendix A 3). The application of input-output theory to this model (see Appendix D 3 a), provides also a good description of the transmission data, as shown by Fig. 3c, and confirms that LER-9 does not directly couple to the spins but, rather, to the hybrid LER-10 polariton.

B. Two spin ensembles coupled to a LER pair: polariton-polariton coupling

Our second study case is illustrated by Fig. 4a (see also Fig. 27 in Appendix D 3 b). Here, LER-1 ($\omega_{r,1}/2\pi = 1.703$ GHz) and LER-2 ($\omega_{r,2}/2\pi = 1.710$ GHz) within a

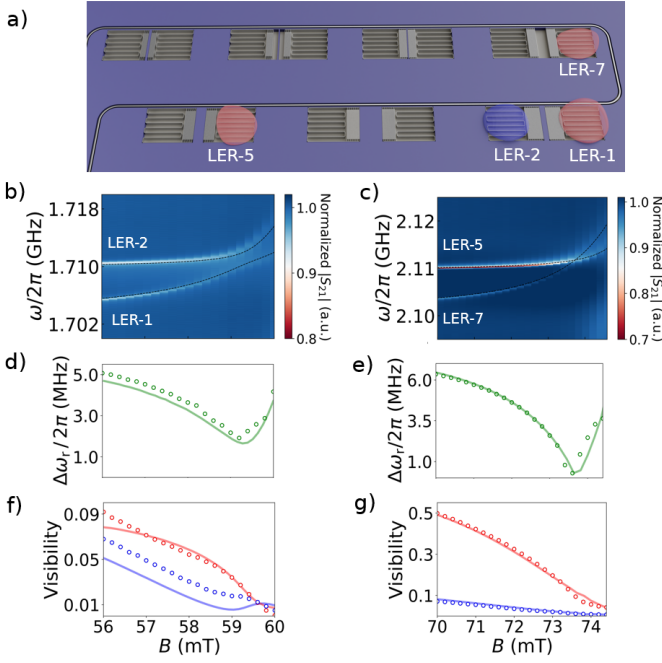


FIG. 4: Experimental setup for polariton-polariton coupling. Two LERs belonging to either a coupled pair (LER-1 and LER-2) or to two different and distant pairs (LER-5 and LER-7) host different molecular spin ensembles (blue: Tripak^- , orange: PTMr). Panels b), d), f) and c), e), g) provide experimental data and simulations obtained for the coupled and the uncoupled LERs, respectively: colour plots of the microwave transmission measured at $T = 11$ mK near the resonances of each spin ensemble with its local LER (b, c); experimental (dots) and theoretical (lines) frequency differences between the two upper polaritons as a function of magnetic field (d, e); experimental (dots) and theoretical (lines) visibilities of these modes as a function of magnetic field (f, g). The fits are based on the model outlined in the text [Eq. (1)] and detailed in Appendix D 1 b, with parameters $G_1/2\pi = 19.5$ MHz, $G_2/2\pi = 8.5$ MHz and $\kappa_{1,2}/2\pi = 1.06$ MHz for the coupled LER pair and $G_7/2\pi = 22$ MHz, $G_5/2\pi = 9.7$ MHz and $\kappa_{5,7}/2\pi = 0$ for the uncoupled LERs.

pair host approximately 5×10^{14} PTMr and Tripak^- radical molecules, respectively. This setup aims to couple distant polaritons via the circuit. For comparison purposes, we have also performed the same study on two different PTMr samples placed onto further distant $\simeq 2.1$ GHz LER-5 and LER-7 belonging to different pairs (Fig. 4a). This allows comparing experimentally the response of a coupled LER pair to that of two uncoupled LERs. Microwave transmission data measured near the spin resonances $\Omega_{S,i} = \omega_{r,i}$ are shown in Figs. 4b and 4c, while results obtained over wider frequency and magnetic field regions are given in Appendices B and D 3 b.

The local spin-photon couplings reach high cooperativity for LER-2 and LER-5 ($G_2/2\pi = 8.5$ MHz,

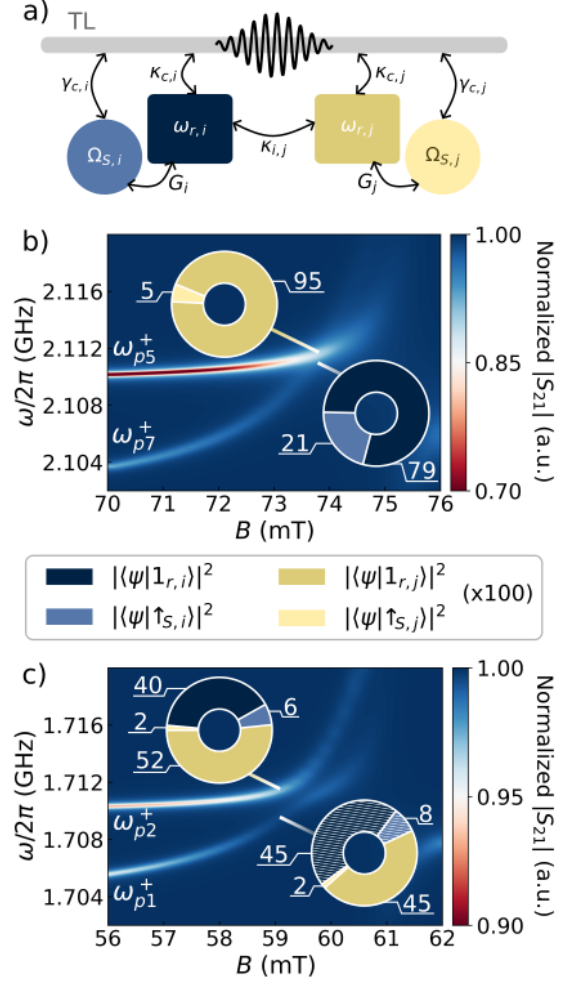


FIG. 5: a) Sketch of the polariton-polariton coupling model showing the main interactions present in the system (1). Details of the eigenstates and of the microwave transmission calculations are described in Appendix D. b) and c) Simulated 2D microwave transmission plots for two uncoupled ($\kappa_{i,j} = 0$) and two coupled ($\kappa_{i,j} = 1.06$ MHz) LERs, respectively. The insets show the probabilities of the single spin and single photon excitation states in each polariton. Striped sectors in the inset of panel c) signal negative probability amplitudes.

$G_5/2\pi = 9.7$ MHz) and the strong coupling regime for LER-1 and LER-7 ($G_1/2\pi = 19.5$ MHz $G_7/2\pi = 22$ MHz). The different coupling strengths and, to a lesser extent, the different spin resonance frequencies of PTMr and Tripak^- (see Fig. 2) allow tuning the upper polariton branches of different LERs relative to each other, eventually bringing them into mutual resonance as shown in Figs. 4b and 4c. In the case of the uncoupled LER-5 and LER-7 (Fig. 4c and 4e), the two branches then simply cross. By contrast, for the two coupled LERs (Fig. 4b and 4d) there is an avoided level crossing with a gap $\Delta\omega_p^+/2\pi \simeq 1.9$ MHz near 59.2 mT. This behaviour resembles the mode splitting of

two identical coupled LERs, shown in Fig. 1c), only here we deal with polaritons and the tuning is achieved in situ by the magnetic field, exploiting their different spin components. By analogy, we conclude that the gap $\Delta\omega_p^+$ is a direct manifestation of the polariton-polariton interaction that allows estimating the coupling constant $J_{1,2}^+/2\pi \simeq \Delta\omega_p^+/4\pi = 0.96$ MHz. Furthermore, near the anticrossing the visibilities of the two coupled polariton branches, shown in Fig. 4f, go through a local minimum and a local maximum, respectively; i.e., the coupled modes become then "brighter" and "darker", which suggests the formation of delocalized photon states with dominantly symmetric and antisymmetric characters. This effect is not observed for the two uncoupled LERs (Fig. 4g).

Hamiltonian (1) helps again in getting a better insight into these results. In this case, and as it's sketched in Fig. 5a, the two LERs interact with a different spin sample, with respective coupling strengths G_i and G_j . As shown in Figs. 4d and 4e, this model accounts for the onset of a finite gap between the two polariton branches when $\kappa_{i,j} \neq 0$, which is given by the following expression:

$$\Delta\omega_p^+ = 2J_{i,j}^+ = 2\kappa_{i,j} \cos \frac{\theta_i}{2} \cos \frac{\theta_j}{2}, \quad (3)$$

where $\theta_i = \tan^{-1}(2G_i/\Delta_i)$, with $\Delta_i = \Omega_{S,i} - \omega_{r,i}$ (and equivalently for LER- j) measure the spin components of the two polaritons. The same model, combined with the input-output formalism that includes the couplings of all components to the readout line (see Fig. 5a and Appendices D 1 b, D 2 and D 3 b for details) describes the overall features observed in the microwave transmission experiments. This is confirmed by comparing the simulations in Figs. 5b and 5c to the experimental results shown in Figs. 4c and 4b, respectively. The model also accounts for the changes in polariton visibilities that take place near the anticrossing (Figs. 4f and 4g). In all these simulations, $\kappa_{i,j}$ is the only free parameter, the rest being obtained from independent fits to the data. The estimated $\kappa_{1,2}/2\pi = 1.06$ MHz turns out to be a factor two smaller than $\kappa_{1,2}/2\pi = 2.4$ MHz obtained from the circuit simulations (Annex A 1).

The simulations also provide information on the nature of the polaritonic states and on how they are modified by their mutual interaction and by external parameters. The probabilities of the polaritons in the basis of local single-photon and single-spin excitations are shown as insets to Figs. 5b and 5c. For $\kappa_{i,j} = 0$, spin and photon excitations hybridize locally, but there are no correlations between 'left' and 'right' excitations. By contrast, for $\kappa_{i,j} \neq 0$ the polaritons acquire finite amplitudes of spin and photon excitations arising from both LERs (Fig. 22 from Appendix D 1 b) when they are brought into resonance by the magnetic field. Near the anticrossing, the photonic component approaches symmetric and antisymmetric combinations of the local photon modes, and the

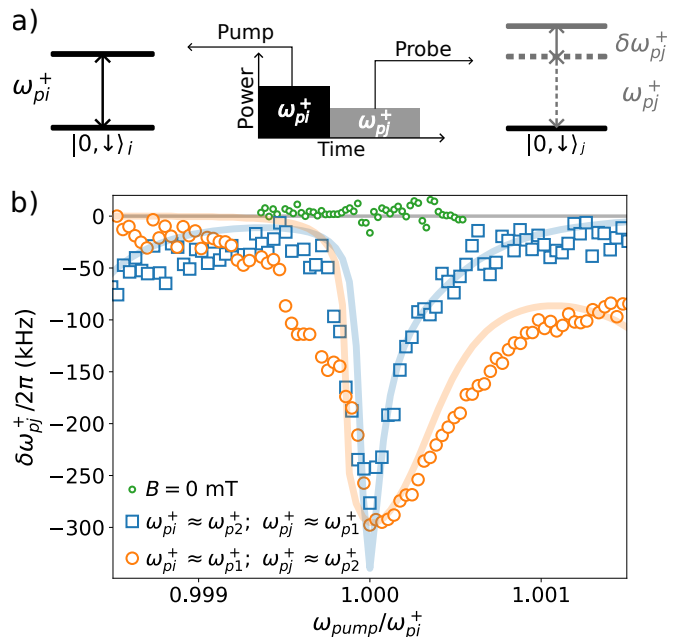


FIG. 6: Polariton-polariton pump-probe measurements. a) Sketch of the measurement protocol. A short high power microwave pulse resonantly excites one polariton at a frequency $\omega_{p,i}^+$. Then, a series of lower power pulses probe the frequency shift $\delta\omega_{p,j}^+$ generated on the other polariton. b) Experimental frequency shift measured at $T = 11$ mK by pumping LER-1 polariton ($\omega_{p,1}^+/2\pi \simeq 1.706$ GHz) and detecting changes in the LER-2 polariton (orange circles) and vice versa (blue open squares). Data measured at $B = 0$, when excitations at both LER correspond to pure photon modes and no dispersive shift is observed, are also shown as green circles. In these experiments LER-1 was coupled to a PTMr spin ensemble whereas LER-2 was coupled to a Tripak⁻ sample. The lines are theoretical predictions for the dynamical response of the system sketched in Fig. 5a obtained by solving the time-dependent master equations as described in [36].

entanglement between these modes becomes then maximum (Fig. 23 in Appendix D 1 b). By contrast, and as discussed in Appendix D 1 b, the opposite limit of far detuned, nearly localized polaritons, leads to a circuit mediated effective transverse interaction $J(S_i^+ S_j^- + S_i^- S_j^+)$ between the excitations of the two spin ensembles. This then resembles the situation met when two spin ensembles couple to just a cavity mode in the dispersive regime [8, 16, 22].

C. Polariton-polariton dispersive readout

The dual character of the polariton excitations and the existence of spin-spin and photon-photon remote correlations can be probed by performing pump-probe

experiments with microwave pulses that use one of the polaritons to sense the excitation of the other one. The protocol and the experimental set-up are sketched in Figs. 6 and Appendix A 5, respectively. A high- power short ‘pump’ pulse resonantly excites a polariton on one side of the LER pair. This is then followed by a set of ‘probe’ pulses with frequencies scanning that of the other polariton that allows detecting any changes in its resonance frequency.

Results of reference experiments performed at zero field, when the LER excitations are pure photonic modes, are shown in Figs. 6 and Appendix C 1. They show no measurable shift, as expected for two coupled resonators, whose frequencies must remain insensitive to changes in their respective populations. By contrast, when $B = 57$ mT, near the avoided level crossing in Fig. 4b, both polaritons acquire a finite spin component (see Fig. 5c). In this case, the initial excitation of one mode, at a frequency $\omega_{p,i}^+$ does generate a measurable shift $\delta\omega_{p,j}^+$ in the frequency $\omega_{p,j}^+$ of the other one. Examples of the readout process and results obtained at different magnetic fields are given in Appendix C 2.

The measurement of the frequency shift can be exploited to perform polariton spectroscopy. For this, ω_{pump} is swept across $\omega_{p,i}^+$. The ensuing $\delta\omega_{p,j}^+$ then maps the distribution of polariton excitation frequencies. The results, shown in Fig. 6b, agree with the polariton line shapes derived from transmission experiments (Fig. 4). These measurements also show that the two polaritons can perform both roles, either as ‘spins’ or as ‘probes’. They’re also in good agreement with theoretical predictions (solid lines in Fig. 6b) that have been obtained by solving the master equations governing the time-dependent response of the coupled system, as described in [36]. These results give further insight into the upper polariton wave functions. We find polariton line widths $\kappa_1^+/2\pi \simeq 0.5$ MHz and $\kappa_2^+/2\pi \simeq 0.2$ MHz, which lie in between the pure photon and spin line widths, as expected. Their values are determined by the ratio G_i/Δ_i . More strongly coupled spins (in this case at LER-1) give then rise to broader polariton excitations.

IV. CONCLUSIONS

In summary, we have tested in different scenarios a modular platform whose basic nodes are hybrid spin-photon polaritons. The results show that each of these nodes can be addressed and read out by quite standard microwave transmission experiments. Besides, they can be deterministically coupled via the circuit, with coupling strengths $\sim \Delta\omega_p^+/2$ that can be made strong enough to overcome polariton losses. This platform opens possibilities to generate and control in situ effective interactions and entanglement between distant spins and photons us-

ing external parameters as ‘control knobs’. In spite of the fact that the LERs mutual capacitive couplings are fixed by the circuit geometry, their effect on the spin and photon polariton components can be tuned by changing the magnetic field, and also driving power (Appendix B 2) or temperature (Appendix B 3). This scheme then offers an alternative route to realize some key elements of quantum circuits such as switches [35] or filters [37], which are based on coupling two or more resonators. In combination with recently developed techniques to enhance the single spin–photon coupling [36], this work contributes to scaling up hybrid quantum technologies based on molecular spins [25–27] by establishing hybrid spin–photon polaritons as addressable nodes in superconducting quantum circuits.

ACKNOWLEDGMENTS

The authors acknowledge useful discussion with M. J. Martínez-Pérez. This work has received support from grants TED2021-131447B-C21, TED2021-131447B-C22, PID2022-140923NB-C21, PID2022-141393OB-I00, CEX2023-001263-S and CEX2023-001286-S funded by MCIN/AEI/10.13039/501100011033, ERDF ‘A way of making Europe’ and ESF ‘Investing in your future’, from the Gobierno de Aragón grant E09-23R-QMAD, from the European Union Horizon 2020 research and innovation programme through FET- OPEN grant FATMOLS-No862893, from the Novo Nordisk Foundation Exploratory Interdisciplinary Synergy Programme 2021 through grant NNF21OC0070832, from QUANTERA project OpTriBits (AEI: PC2024-153480), and from the Spanish Ministry for Digital Transformation and Civil Service and Next Generation EU through the Quantum Spain project (Digital Spain 2026 Agenda). It also forms part of the Advanced Materials and Quantum Communication programmes with funding from European Union Next Generation EU (PRTR-C17.I1), MCIN, Gobierno de Aragón, and CSIC (QTEP-PT-001). D.P. acknowledges the financial support of the National Science Centre Poland within the Opus project 2020/37/B/ST5/02735

Appendix A: Experimental details

1. Circuit design and fabrication

The platform used in the experiments, shown in Fig. 1a, consists of a superconducting chip containing a single impedance-matched transmission line and 14 side-coupled Lumped Element Resonators (LERs). LERs are circuits made of an inductor L and a capacitor C connected in series, as shown in Fig. 7a. The capacitor consists of several interdigitated fingers. Its capacitance is defined by the finger length, width, and separation. Regarding the inductor, a meander-like design is used. The

| LER | $\omega_r/2\pi$ (GHz) | $\kappa/2\pi$ (kHz) | $\kappa_c/2\pi$ (kHz) | Sim. $\kappa_{i,j}/2\pi$ (MHz) | Exp. $\kappa_{i,j}/2\pi$ (MHz) |
|-----|-----------------------|---------------------|-----------------------|--------------------------------|--------------------------------|
| 1 | 1.703 | 91 | 18.5 | 2.4 | 1.06 |
| 2 | 1.710 | 103 | 7 | | |
| 3 | 1.904 | 68 | 52 | 0.33 | - |
| 4 | 1.926 | 40 | 15 | | |
| 5 | 2.109 | 80 | 62 | 0.965 | - |
| 6 | 2.147 | 244 | 22 | | |
| 7 | 2.112 | 91 | 18 | 30 | - |
| 8 | 2.187 | 184 | 29 | | |
| 9 | 2.719 | 61 | 50 | 5.75 | 6.5 |
| 10 | 2.729 | 44 | 31 | | |
| 11 | 2.645 | 213 | 28 | 9 | - |
| 12 | 2.665 | 62 | 23 | | |
| 13 | 3.274 | 185 | 22 | 2.66 | - |
| 14 | 3.291 | 130 | 29 | | |

TABLE I: Characteristic parameters of the 14 LER resonances obtained by fitting microwave transmission data to the theoretical model described in Appendix D. Here, ‘Sim. $\kappa_{i,j}$ ’ is the capacitive coupling strength between the two LERs within each pair, determined by simulating the microwave transmission using Sonnet, as shown in Fig. 7b, while ‘Exp. $\kappa_{i,j}$ ’ denotes the coupling strength obtained from experiments performed for LER-1 and LER-2 and for LER-9 and LER-10. For these two LER pairs, the other parameters have been adjusted using the experimental $\kappa_{i,j}$, whereas for the rest the simulated $\kappa_{i,j}$ was used.

inductance is mainly determined by the length and width of the superconducting metal stripe.

The resonance frequency of each LER- i is $\omega_{r,i} = 1/\sqrt{LC}$, with $i = 1, \dots, 14$. Every LER in the chip has a slightly different frequency. For this purpose, all LERs have the same $L \simeq 6$ nH whereas C_i is varied by changing the number of fingers and their length. The 7-turn inductor is made of a 4μ m wide strip with the dimensions indicated in Fig. 7a. The capacitors contain from 10 to 26, 6μ m wide fingers separated by 6μ m gaps. Their length varies from 690 to 750μ m. The geometrical capacitance (without taking into account any parasitic capacitance) ranges between 0.99 pF and 0.28 pF. The coupling to the feed-line $\kappa_{c,i}$ depends the distance of the resonator to the transmission line. This chip was designed for coupling values $\kappa_{c,i} \approx 20 - 30$ kHz.

LERs in the chip are distributed in pairs. LERs (i, j) forming a pair are oriented with their capacitors facing each other, as illustrated by Fig. 7. This geometry induces a capacitive coupling whose strength $\kappa_{i,j}$ is different for each pair and depends on the distance between them.

The LER and readout line geometries were designed using AutoCAD. The microwave transmission through the line near the LER resonances was simulated using Sonnet. When both LERs of a pair are identical the frequency splitting between the two resonant modes $\Delta\omega_r = 2\kappa_{i,j}$ (Fig. 7b), which allows estimating the capacitive coupling strength. We design the circuit such that $\kappa_{i,j}/2\pi$ ranges from 0.3 to 30 MHz. In order to allow individually addressing the LERs within each pair, they

are detuned by approximately 20 – 30 MHz, such that the ‘dispersive’ condition $\Delta\omega_r > \kappa_{i,j}$ is approximately fulfilled. Moreover, nearest LER pairs are separated by 0.6 mm to 1 mm and detuned 250 MHz from each other to prevent unwanted crosstalk.

The chip fabrication process starts with the pretreatment of a 275μ m thick Si substrate in a 1 % hydrofluoric acid bath to remove the native silicon oxide layer. A 125 nm thick superconducting NbTiN film is then deposited onto the Si substrate by using confocal DC AJA magnetron sputtering, with a chamber base pressure below 2×10^{-8} Torr. The deposition conditions were controlled with an argon flow of 15 sccm and a nitrogen flow of 1 sccm as a plasma processing gases, maintaining a chamber pressure of 2 mTorr and a power setting of 200 W. These conditions lead to a deposition rate of $1.21 \text{ \AA}/s$. Afterwards, maskless laser writer lithography with a MicroWriter ML3 Pro system is employed to pattern the chip design onto the NbTiN film. For this, a layer of negative photoresist (AZ2070) is spin-coated onto the surface and exposed to a 405 nm laser at room temperature. Following the development of the resist, reactive ion etching is performed. The etching gases, SF₆ and Ar, were flowed at rates of 20 sccm and 10 sccm, respectively. The process operated at 75 W of RF power and a chamber pressure of 10 mTorr. The process concludes with the removal of the remaining photoresist by boiling in acetone, followed by rinsing with isopropanol.

2. Molecular integration and characterization

The PTMr and Tripak⁻ organic free radical molecules were dissolved in chlorobenzene, with concentrations ranging from 0.08 to 8 mM, together with polystyrene. Then, 0.1μ l drops were transferred onto different parts of the circuit, namely the LER inductors or the transmission line, and left dry under red light, as shown in Fig. 8. The resulting solid deposits are very stable at ambient conditions and contain a nominal spin number N determined by concentration, namely $N \simeq 5 \times 10^{12}$, $N \simeq 5 \times 10^{13}$ and $N \simeq 5 \times 10^{14}$ for, respectively, 0.08 mM, 0.8 mM and 8 mM solutions. Although polystyrene prevents aggregation of the free radical molecules, the dry deposits are still quite inhomogeneous, which leads to different spin-photon couplings even for drops with nominally the same number of spins. In order to cover different LERs within a pair with a different free radical sample, the drops were landed onto the region separating two neighbor inductors from different LER pairs. An example is shown in Fig. 27 below.

The spin resonance frequencies Ω_S of both samples were characterized by broadband magnetic spectroscopy, performed by measuring the microwave transmission through a superconducting waveguide coupled to a molecular deposit [33, 34]. Results are shown in Figs. 2c,d and 9a,b. Figures 9c and d show that $\Omega_S \simeq g\mu_B SB/\hbar$. From the linear slope we find $g = 2.001$

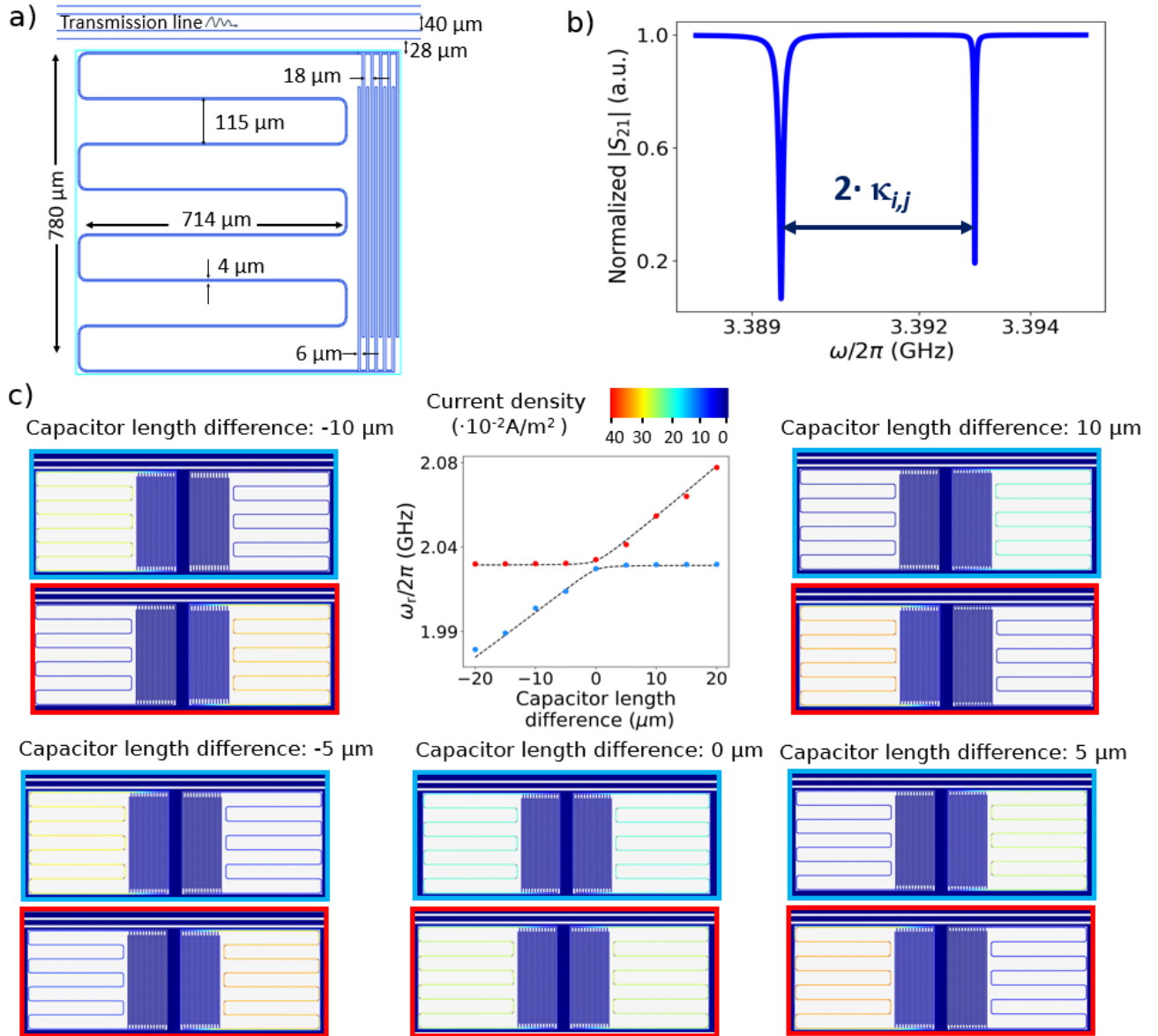


FIG. 7: a) Sketch of a superconducting LER showing the LC circuit dimensions. b) Sonnet simulation of two capacitively coupled LERs. The microwave transmission through the readout line, normalized to the maximum transmission, shows two dips that correspond to absorption by symmetric and antisymmetric resonant modes with frequencies separated by twice the coupling constant $\kappa_{i,j}$. c) Single-photon current density maps simulated with Sonnet for different values of the detuning between the bare LER frequencies. The modes become more localized as the detuning is increased.

for PTMr and $g = 2.003$ for Tripak⁻. When they are coupled to the two LERs within a pair, the slightly different magnetic responses of PTMr and Tripak⁻ contribute to making their respective polariton frequencies tuneable relative to each other (Fig. 4).

3. Cryogenic setup

Experiments reported in this paper are performed at temperatures $T \geq 11$ mK, by thermally anchoring the chips to the mixing chamber of an ³He-⁴He cryo-free dilution refrigerator (Fig. 10a). A copper cold finger (Fig. 10b) places the chip at the centre of a 1 T axial superconducting magnet (Fig. 10c). The magnetic field \vec{B} is applied along the \hat{z} axis of the laboratory reference frame, which is parallel to the chip's readout waveguide.

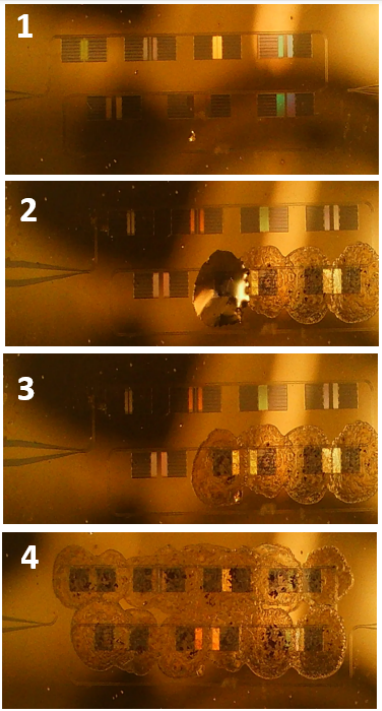


FIG. 8: Optical microscopy images showing different steps in the deposition of Tripak⁻ from a 0.8 mM solution in chlorobenzene. Starting from the bare chip (panel 1), in each step, a new drop is deposited on top of a LER inductor (panel 2) using a micropipette and then left dry under red light (panel 3) until all LER inductors are covered with the desired sample (panel 4). The dry deposits consist of the free radical molecules dispersed in polystyrene

Cryogenic coaxial lines transmit the input and output microwave signals. The input signal was attenuated by two or more -10 dB attenuators before reaching the chip. The output signal was amplified $+30$ dBm at ~ 4 K with a low-noise cryogenic amplifier.

4. Microwave transmission experiments

The continuous wave (cw) microwave transmission through the device was measured using a Vector Network Analyser (VNA). The VNA generates a microwave signal, with a frequency $\omega/2\pi$ ranging from 0.01 GHz up to 14 GHz, which is fed into the chip's readout line. The output signal is then amplified at 4 K and detected by the VNA to determine the S_{21} transmission parameter.

Illustrative microwave transmission results, measured at $T = 11$ mK and normalized to the maximum transmission, are shown in Fig. 11 and Table I. The LER resonances give rise to very narrow dips in transmission that can be described by the following expression:

$$S_{21} = 1 - \frac{\kappa_c}{i(\omega_r - \omega) + \kappa} \quad (\text{A1})$$

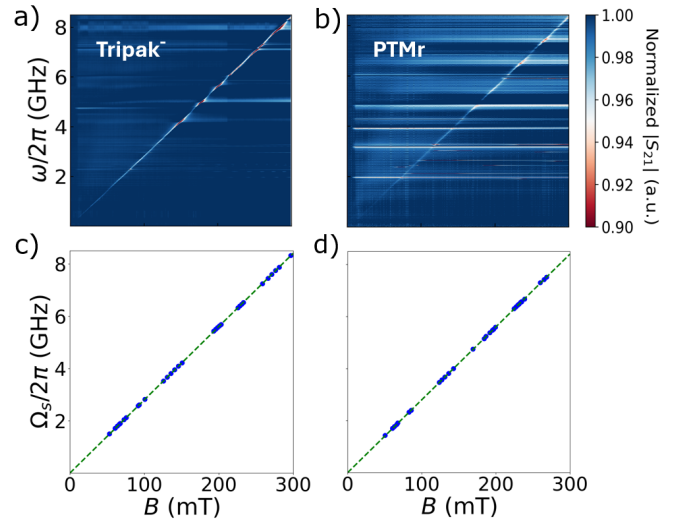


FIG. 9: Spin characterization by broadband magnetic spectroscopy. Two-dimensional plots of the microwave transmission of a superconducting waveguide coupled to Tripak⁻ (a) and PTMr (b), measured at $T = 11$ mK as a function of frequency and magnetic field. Magnetic field dependence of the spin resonance frequency for Tripak⁻ (c) and PTMr (d). The lines are least-squared fits based on $\Omega_S = g\mu_B B/\hbar$ giving $g = 2.003$ for Tripak⁻ and $g = 2.001$ for PTMr.

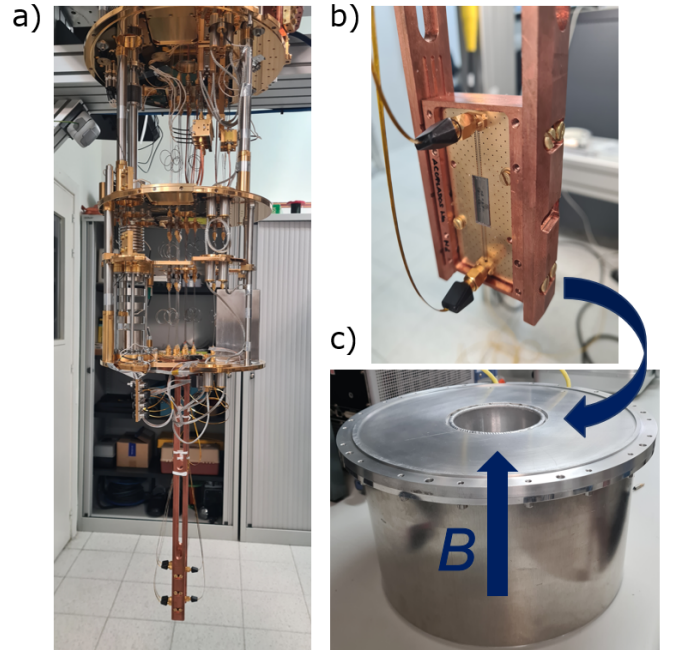


FIG. 10: Microwave transmission setup. a) Image of the cryo-free ^3He - ^4He dilution refrigerator used for both the cw microwave transmission experiments and the pump-probe experiments with microwave pulses. b) Cold finger hosting the superconducting chip at the center of the 1 T cryo-free superconducting magnet c). The magnetic field \vec{B} is applied in the chip's plane, parallel to the readout transmission line.

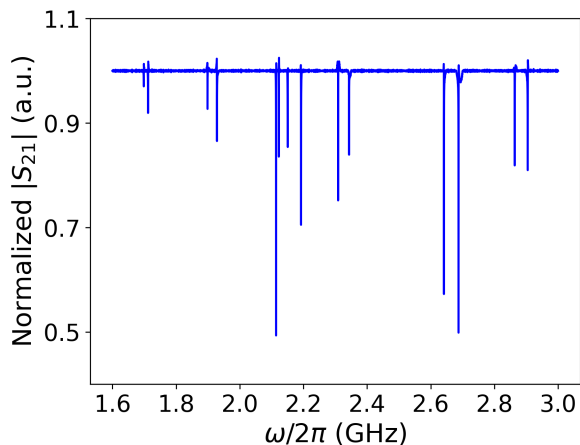


FIG. 11: Microwave transmission through the readout line of the device shown in Fig. 1a, measured at $B = 0$ and $T = 11$ mK.

where κ is the LER photon decay rate and κ_c is the coupling rate to the readout line.

5. Experiments with microwave pulses

Figure 12 illustrates the microwave pulse generation and detection stages used in the pump probe experiments. It consists of a digital Arbitrary Wave Generator (AWG) that sends short and high power pump pulses to resonantly excite either the spins or the polariton modes. These are followed by a train of lower power readout pulses to detect any changes produced in the LER or polariton modes. A microwave switch, triggered by the AWG, feeds excitation and readout pulses into separate lines at the initial room temperature stage. The probe signal then splits into a local oscillator reference for the readout stage (LO) and the signal that is fed into the cryogenic stage. Pump and probe signals are combined again into a single physical line and fed through the same port of the cryostat. At the output of the cryogenic stage, a second switch deviates the pump pulse to a fast microwave oscilloscope in order to avoid damaging the detection electronics. The readout pulse is guided to an IQ mixer, fed with the LO and RF signals, that extracts the two RF quadrature components. These components are then digitalized by the oscilloscope and sent to the computer for post-processing.

Appendix B: Supplementary cw microwave transmission data

1. Coupled *vs* uncoupled LERs

Figures 13a and 13b show the results of cw microwave transmission measurements for LER-1 and LER-2, and

for LER-5 and LER-7. As it is discussed in Section III B above, the former belong to a coupled pair, whereas the latter belong to two different pairs, thus they are mutually uncoupled. All these LERs host free-radical deposits with $N \sim 5 \times 10^{14}$ spins. The plots show transmission data measured over wider frequency and magnetic field regions than those shown in Fig. 4. They confirm the anticrossing occurring between the upper polariton branches of the two coupled LER-1 and LER-2. The gap $\Delta\omega_p^+$ reflects the polariton-polariton coupling generated by the circuit. By contrast, when the the polariton branches of uncoupled LER-5 and LER-7 are brought into resonance by the magnetic field, they simply cross, thus $\Delta\omega_p^+ = 0$. These data show also that the two lower polaritons, which become visible in transmission at higher magnetic fields ($B \gtrsim 75$ mT), do not merge for any of these LER pairs, thus no polariton-polariton interaction effects on transmission are observed in this case.

2. Power dependence of the microwave transmission and the spin-photon coupling

Continuous wave microwave transmission measurements were performed for different input powers. Illustrative results, obtained for 3.274 GHz LER-13 coupled to $N \sim 5 \times 10^{13}$ Tripak⁻ molecules, are shown in Fig. 14a. Typical signatures characterizing the resonant collective coupling to the molecular spins are observed for all input powers. Yet, they become less visible with increasing power, suggesting that the effective spin-photon strength G_{13} decreases. This is confirmed by the data of Fig. 14b, which shows G_{13} , determined by using input-output theory, as a function of power. Data measured for three other LERs coupled to either Tripak⁻ or PTMr deposits of similar size, show the same qualitative behavior. A drop in the effective G_i is expected as the number of photon excitations in each LER increases, approaching the number of spins N .

Figure 15 shows results measured near the resonance frequencies of LERs-1 and 2, which host larger ($N \sim 5 \times 10^{14}$) PTMr and Tripak⁻ deposits, respectively. In this case, the number of photons in both LERs remains low as compared to N , and no significant effect of increasing power is observed in either G_1 , G_2 or the polariton-polariton anticrossing $\Delta\omega_p^+$.

3. Temperature dependence of the microwave transmission and the spin-photon coupling

The interaction between the spins and their host LERs depends on the population of the spin- up and spin-down states, thus it is also affected by temperature. Increasing T reduces the spin polarization at any magnetic field, leading to a decrease in G_i given by the following expression:

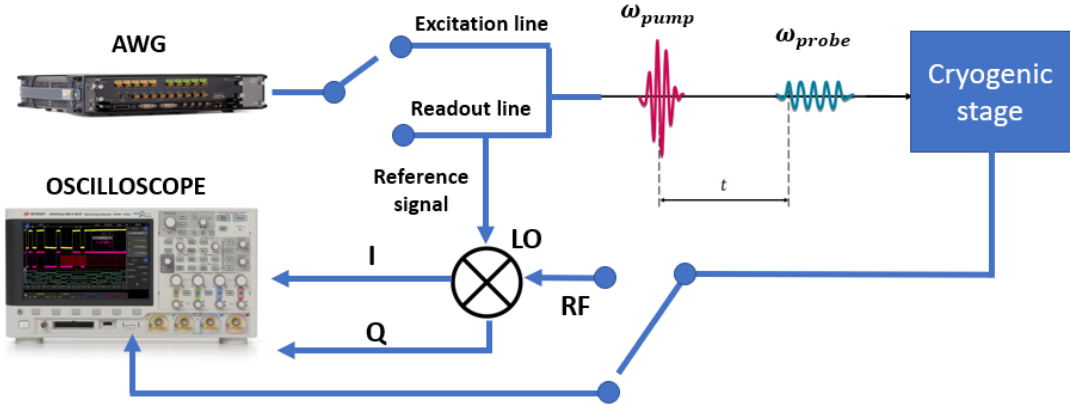


FIG. 12: Microwave pulse generation and detection stages. A fully digital microwave AWG generates the excitation and readout signals. The readout signal is first down converted by a synchronous IQ mixer and then its two quadrature components are digitalized by a fast digital oscilloscope.

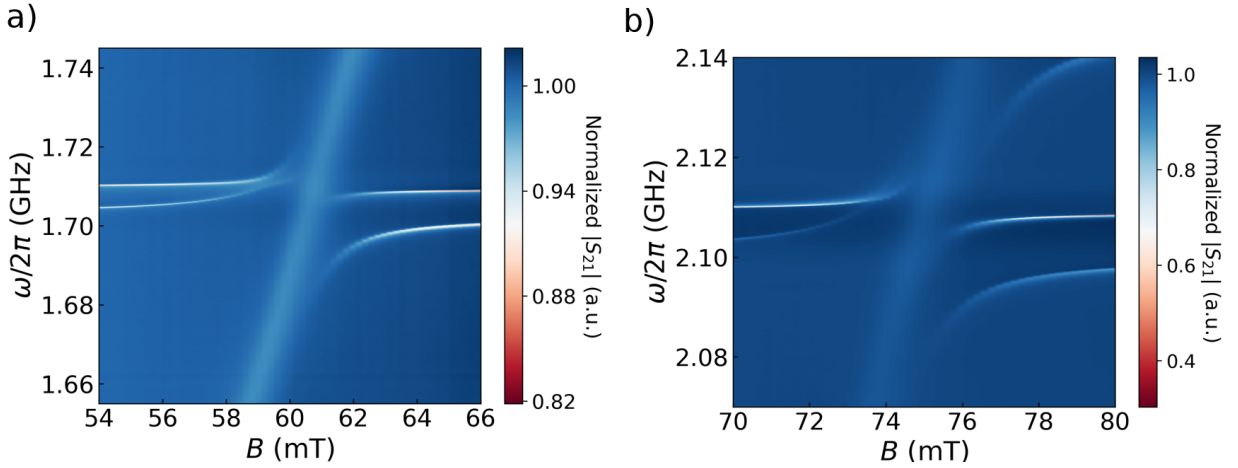


FIG. 13: $2D$ plot of the microwave transmission measured at $T = 11$ mK near the resonance frequencies of: a) LER-1 (coupled to PTMr) and LER-2 (coupled to Tripak^-) belonging to a coupled pair; b) LER-5 (coupled to PTMr) and LER-7 (coupled to PTMr), belonging to different pairs, thus being mutually uncoupled. The signal arising from the direct coupling of spins to the readout transmission line is visible and gives in situ information on the spin resonance frequency.

$$G_i(T) = G_i(0) \sqrt{\tanh\left(\frac{g\mu_B B S}{k_B T}\right)} \quad (\text{B1})$$

Figure 16a shows microwave transmission data measured for the coupled LERs-1 and 2 at four different temperatures. It follows that both the local spin-photon coupling and the mutual polariton-polariton coupling depend on T . The decrease in G_i with increasing T , shown in Fig. 16b, also modifies the relative detuning between the two polariton branches, shifting the polariton-polariton anticrossing towards higher B . In addition, the gap $\Delta\omega_{p+}$, shown in Fig. 16c, gets reduced until it becomes undetectable for $T \geq 500$ mK. The fact that the dependence of G_i with T is weaker than that predicted by Eq. (B1), as shown in Fig. 16b, suggests a non-perfect thermalization of the samples, in particular that

of Tripak^- , below 100 mK or the influence of antiferromagnetic interactions between the different free radicals, which is likely in concentrated samples [34].

Appendix C: Time resolved pump-probe experiments

This section describes results of pump-probe experiments that explore three scenarios, corresponding to excitations of different nature: pure photons, hybrid spin-photon polaritons and pure spins.

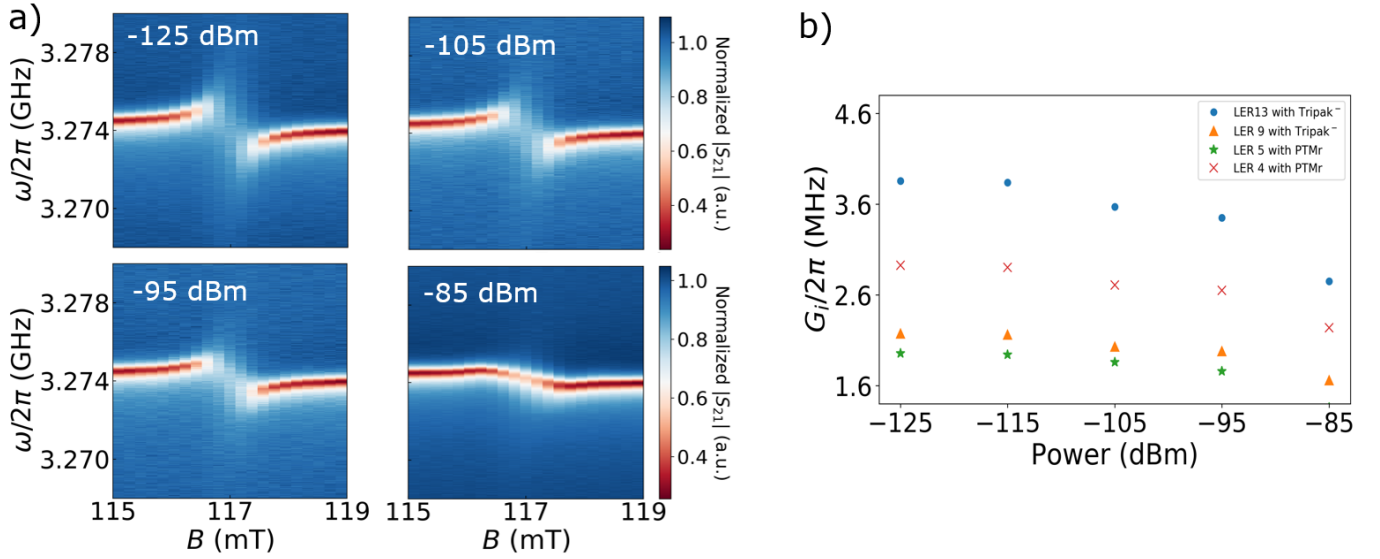


FIG. 14: a) 2D microwave transmission plots measured, at $T = 11$ mK and for different input powers, near the resonance of LER-13 with $N \sim 5 \times 10^{13}$ Tripak⁻ spins. The avoided level crossing associated with the collective spin-photon coupling gradually decreases as the input power is increased. b) Power dependence of the spin-photon coupling strength G_i derived from microwave transmission data using input-output theory. Data are given for LER-13 and LER-9, hosting $N \sim 5 \times 10^{13}$ Tripak⁻ molecules, and for LER-5 and LER-4, hosting $N \sim 5 \times 10^{13}$ PTMr molecules.

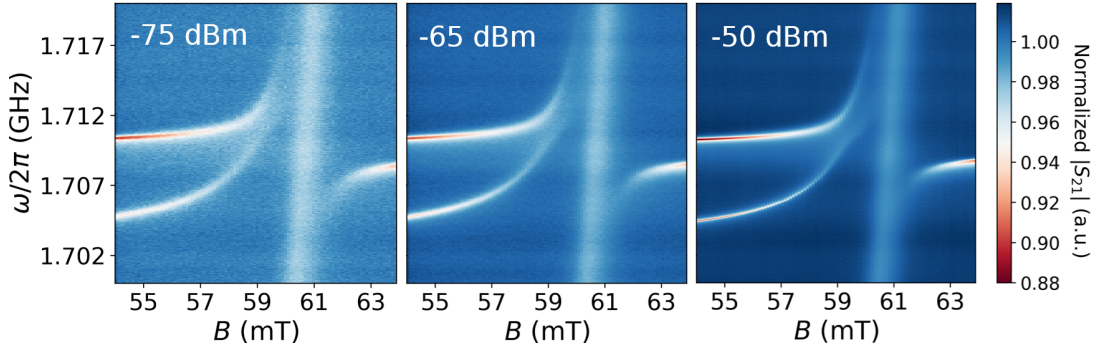


FIG. 15: 2D microwave transmission plots measured, at $T = 11$ mK and for three different input powers, near the resonances of LER-1 and LER-2 with $N \sim 5 \times 10^{14}$ PTMr and Tripak⁻ organic free-radicals, respectively. The data show also the signal arising from the direct coupling of the molecular spins to the readout transmission line. This signal bears evidence of their paramagnetic behaviour. The results show no significant changes in either the local spin-photon couplings or the polariton-polariton anticrossing with increasing power, likely because N remains much larger than the number of photon excitations in both LERs.

1. Photon-photon readout experiments

At $B = 0$ the excitations of two mutually detuned and coupled LERs are photons localized on either of them. Since the two systems are purely harmonic, changes in the photon population of one LER shouldn't generate any shift in the resonance frequency of the other one. The experiments were performed on the pair formed by LER-1 and LER-2. Illustrative results of exciting LER-1 and reading out the frequency changes in LER-2 are shown in Fig. 17a-c. No noticeable shift in $\omega_{r,2}$ is ob-

served. Still, some microwave transmission oscillations appear when the pump frequency matches $\omega_{r,1}$ (Fig. 17a), which become more noticeable in the microwave standard deviation plot shown in Fig. 17d. A plausible explanation of this effect is as follows. When $\omega_{\text{pump}} \simeq \omega_{r,1}$, LER-1 gets charged and then it starts decaying as soon as the pumping pulse ends. Some of the emitted photons reach LER-2 through the readout transmission line. However, since $\omega_{r,2} \neq \omega_{r,1}$, the excitation of LER-2 is incomplete and, besides, it oscillates with $\omega_{\text{pump}} - \omega_{r,2}$, which reflects itself in the transmission through the readout line.

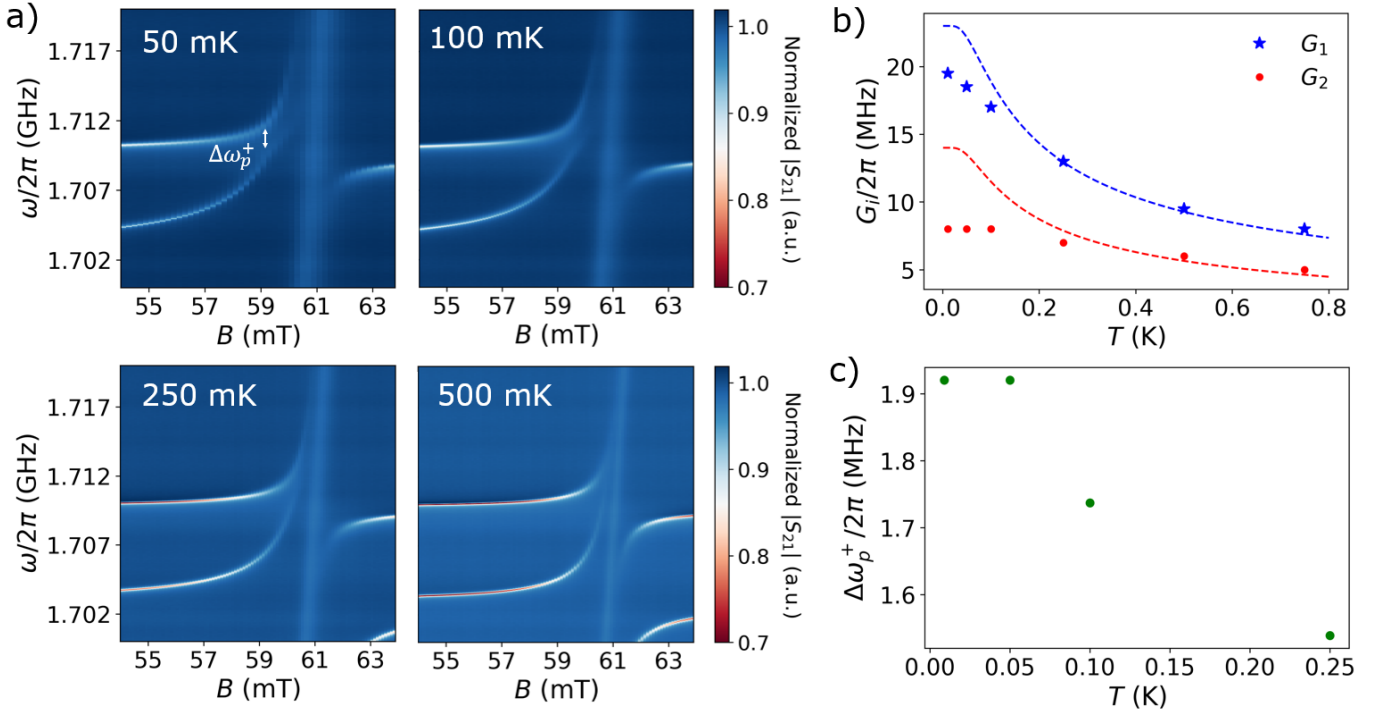


FIG. 16: a) 2D transmission plots near the LER-1 and LER-2 resonances measured at different temperatures. b) Temperature dependence of the collective coupling of each spin sample to photon modes of its host LER (G_1 and G_2 for LER-1 and LER-2, respectively). The lines are least-square fits based on Eq. (B1), which describes the dependence of G_i on spin polarization. c) Temperature dependence of the splitting $\Delta\omega_p^+$ between the two upper polariton branches, which parametrizes the remote polariton-polariton coupling. Notice that, as shown in a), the avoided level crossing between these polariton branches shifts to higher magnetic field values as T increases. At $T = 500$ mK the anticrossing is no longer detectable.

2. Polariton-polariton readout experiments

We next consider pump-probe experiments performed on the same pair formed by LER-1, coupled to $N \sim 5 \times 10^{14}$ PTMr molecules, and LER-2, coupled to $N \sim 5 \times 10^{14}$ Tripak⁻ molecules, at $B = 54$ mT and at $B = 64$ mT, when the spins are still relatively far from resonance with either LER (see Fig. 13a). Therefore, since $(\omega_{r,2} - \omega_{r,1})/2\pi \simeq 7$ MHz is much larger than $\kappa_{1,2}/2\pi \sim 1$ MHz, the upper polaritons consist mainly of photons localized at either LER-1 or LER-2. However, contrary to what happens at $B = 0$, the local spin-photon couplings G_1 and G_2 do still confer to them a tiny spin component and make their frequencies, $\omega_{p,1}^+$ and $\omega_{p,2}^+$, depend on B . The excitation of, say, the upper LER-1 polariton induces then a local spin polarization change that, via the capacitive coupling $\kappa_{1,2}$, must generate a shift in the frequency ω_p^+ of the upper LER-2 polariton.

An example of this shift is shown in Fig. 18a, which gives the LER-2 resonance recorded at $B = 54$ mT before (‘reference’ data) and after the resonant excitation of LER-1 by a 50 μ s long ~ -7 dBm squared pump pulse. The readout is performed by sending a train of one hundred 20 μ s long pulses with frequencies spanning $\omega_{p,2}^+$. The results show a neat shift in $\omega_{p,2}^+$ with respect to

the reference data. The negative sign of $\delta\omega_{p,2}^+$ is due to the negative detuning of the spins with respect to LER-1 (i.e. $\Omega_{S,1} < \omega_{p,1}^+$, see Fig. 13a). Data measured at $B = 64$ mT, using the same protocol at the corresponding polariton frequencies, show instead a positive $\delta\omega_{p,2}^+$ (Fig. 18b) because then $\Omega_{S,1} > \omega_{p,1}^+$.

As discussed in Section C2 above, the roles of the two polaritons can be reversed. Then, we can also use polaritons from LER-1 to readout polariton excitations at LER-2 and, by varying the excitation frequency, obtain spectroscopy information of both polaritonic branches. Results obtained at $B = 54$ mT (leading to negative frequency shifts) are shown in Figs. 18c and 18d, whereas data measured at $B = 64$ mT (leading to positive frequency shifts) are shown in Figs. 18e and 18f. These results confirm also that the polariton line width $\kappa_{p,i}$ depends on G_i and on magnetic field, which combine to determine the degree of spin-photon hybridization.

3. Spin readout and relaxation measurement

Finally, we consider the more conventional spin readout experiments, in which spin excitations are detected via the shift in the frequency of their host LER. There-

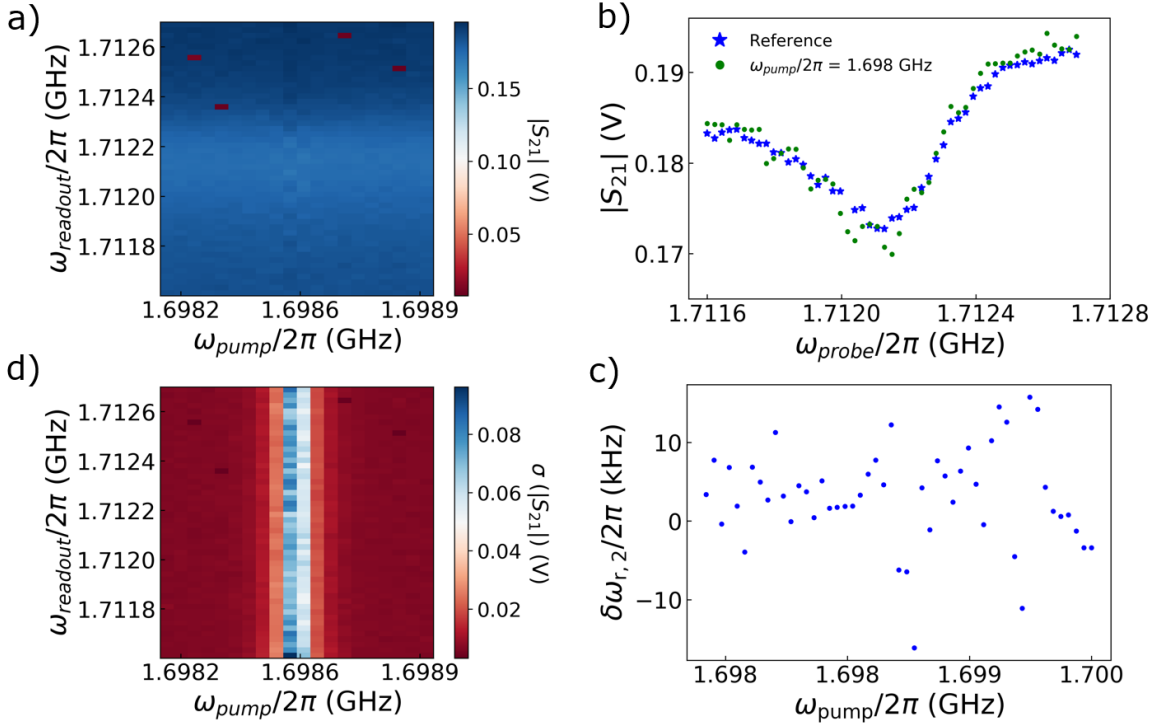


FIG. 17: Pump-probe photon-photon experiments performed at $B = 0$ on LERs 1 and 2. a) 2D plot of the microwave transmission measured near $\omega_{r,2}$ after pumping at frequencies close to $\omega_{r,1}$. b) Example of LER-2 resonance measured with and without (reference) pumping on LER-1. c) Dependence of the LER-2 frequency shift $\delta\omega_{r,2}$ as a function of the pumping frequency. d) Standard deviation of the transmission amplitude in a).

fore, these experiments do not involve any non-local interaction, but are driven by the local spin photon couplings G_1 . Experiments were performed for LER-1 and LER-2 at $B = 66$ mT, using the same protocol described above for the ‘polariton-polariton’ experiments. Only, here the excitation frequency $\sim \Omega_{S,i}$ and the readout is performed by recording the resonance of the same LER- i . These experiments allow estimating the spin relaxation time T_1 of both samples (PTMr and Tripak⁻). For this, we measure the resonance shift for increasing delay times t between the pump and readout pulses. The results are shown in Fig. 19.

The decay of $\delta\omega_{r,i}$ with increasing t is non exponential, likely reflecting a distribution in T_1 values associated with significant spin-spin interactions in these, quite concentrated, samples. In order to estimate T_1 , we fit the experimental data using an stretched exponential function:

$$\delta\omega_{r,i}(t) = \delta\omega_{r,i}(0)e^{-(t/T_1)^x}, \quad (\text{C1})$$

where the exponent $x \simeq 0.3$ accounts for the distribution in relaxation times. We find $T_1 \simeq 0.2$ s for PTMr and $T_1 \simeq 0.024$ s for Tripak⁻.

Appendix D: Theoretical model for polariton-polariton coupling and analysis of microwave transmission experiments

1. Theoretical model: hybrid modules and their coupling

In this section, we present a theoretical framework that describes the interactions within a LER-spin ensemble hybrid system, its energies and wavefunctions, and how these are modified by its coupling to another hybrid module and by external parameters, mainly the magnetic field. The system under study is sketched in Fig. 5a. It includes a LER pair, hereafter labelled generically as LER-1 and LER-2, with bare resonance frequencies $\omega_{r,1}$ and $\omega_{r,2}$. Each LER can host a different spin ensemble, giving rise to local collective spin-photon couplings G_1 and G_2 . We also denote by $\kappa_{c,1}$ and $\kappa_{c,2}$ the couplings of these LERs to the readout line and by $\kappa_{1,2}$ the mutual capacitive coupling between them (see Fig. 7). The Hamiltonian describing this system is given by

$$\mathcal{H} = \mathcal{H}_0 + \mathcal{H}_{\text{sr}} + \mathcal{H}_{\text{rr}}, \quad (\text{D1})$$

where

$$\mathcal{H}_0 = \sum_{j=1}^2 \left(\omega_{r,j} a_j^\dagger a_j + \Omega_{S,j} S_j^z \right), \quad (\text{D2})$$

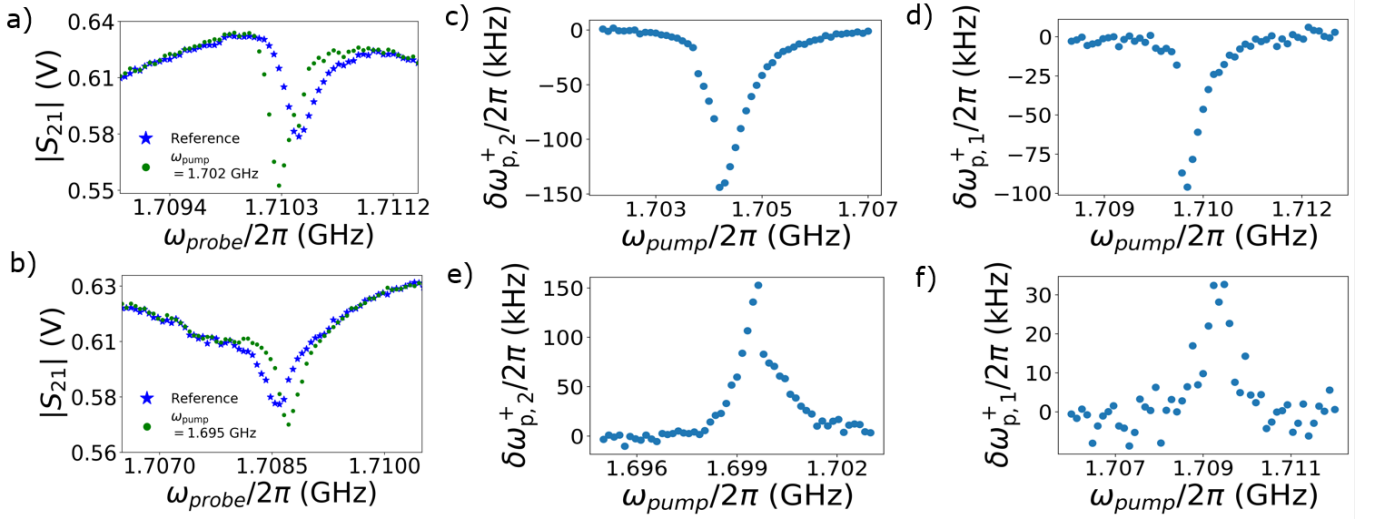


FIG. 18: Polariton-polariton readout measurements performed on the coupled LER-1 (coupled to $N \sim 5 \times 10^{14}$ PTMr spins) and LER-2 (coupled to $N \sim 5 \times 10^{14}$ Tripak⁻ free radical molecules). a) and b) show the LER-2 upper polariton resonance measured at $B = 54$ mT and $B = 64$ mT, respectively, after the resonant excitation of the LER-1 upper polariton, compared to the reference data (measured without any previous excitation pulse). c) and d), spectra of the LER-1 and the LER-2 upper polaritons, respectively, measured at $B = 54$ mT using the frequency shift $\delta\omega_{p,j}^+$, with $j = 2, 1$, respectively. The polariton line widths derived from these data are, approximately, $\kappa_{p,1}/2\pi \simeq 0.73$ MHz and $\kappa_{p,2}/2\pi \simeq 0.34$ MHz. e) and f) Same as in c) and d) for $B = 64$ mT. Notice the change in the sign of $\delta\omega_{p,j}^+$. The polariton line widths at this field are $\kappa_{p,1}/2\pi \simeq 1.2$ MHz and $\kappa_{p,2}/2\pi \simeq 0.68$ MHz.

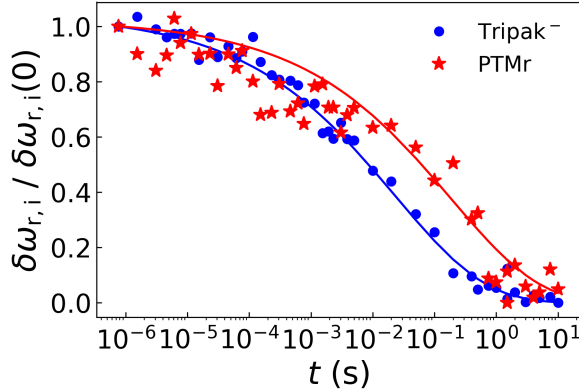


FIG. 19: Decay of the resonance frequency shift generated by the resonant spin excitation of PTMr (coupled to LER-1) and Tripak⁻ (coupled to LER-2) spins at $B = 66$ mT. The solid lines are least-square fits based on a stretched exponential [Eq. (C1)] with the parameters given in the text.

$$\mathcal{H}_{\text{sr}} = \sum_{j=1}^2 G_j \left(a_j S_j^+ + a_j^\dagger S_j^- \right) \quad (\text{D3})$$

and

$$\mathcal{H}_{\text{rr}} = \kappa_{1,2} \left(a_1^\dagger a_2 + a_1 a_2^\dagger \right). \quad (\text{D4})$$

In the expressions above, a_j and a_j^\dagger represent the photon annihilation and creation operators, respectively, in each cavity $j = 1, 2$, S_j^α , with $\alpha = z, +, -$, represent the conventional spin-1/2 operators and the spin resonance frequency is related to the magnetic field through $\Omega_{S,j} = g_j \mu_B B$, in agreement with the experiments shown in Fig. 9.

Before describing situations characterized by a finite interaction between the two LERs, given by Eq. (D4), we first consider the limit of vanishing $\kappa_{1,2}$, which allows introducing mathematically the central single object of this work, the spin polaritons. These are single light and matter excitations that arise as eigenstates of the Hamiltonian formed by $\mathcal{H}_0 + \mathcal{H}_{\text{sr}}$. In order to write these eigenstates down, let us first define our basis as $\{|n_1, m_1^z, n_2, m_2^z\rangle\}$ where n_j indicates the number of photons in LER j (here, either 0 or 1) and $m_j^z = \{\uparrow, \downarrow\}$ is the spin polarization along its quantization axis z . Let $|\downarrow\rangle$ be the ground state of the spin subsystem. Now, the polaritons of module $j \neq i$ are defined by the following states

$$|p_j^+\rangle = \left(\sin \frac{\theta_j}{2} |0, \uparrow\rangle_j + \cos \frac{\theta_j}{2} |1, \downarrow\rangle_j \right) |0, \downarrow\rangle_i, \quad (\text{D5a})$$

$$|p_j^-\rangle = \left(\cos \frac{\theta_j}{2} |0, \uparrow\rangle_j - \sin \frac{\theta_j}{2} |1, \downarrow\rangle_j \right) |0, \downarrow\rangle_i, \quad (\text{D5b})$$

and similarly for the polaritons of module i . Here, $\theta_j = \tan^{-1}(2G_j/\Delta_j)$ and $\Delta_j = (\Omega_{S,j} - \omega_{r,j})$ are the usual parameters that characterize the spin-photon hybridization within a Jaynes-Cummings model [38]. The maxi-

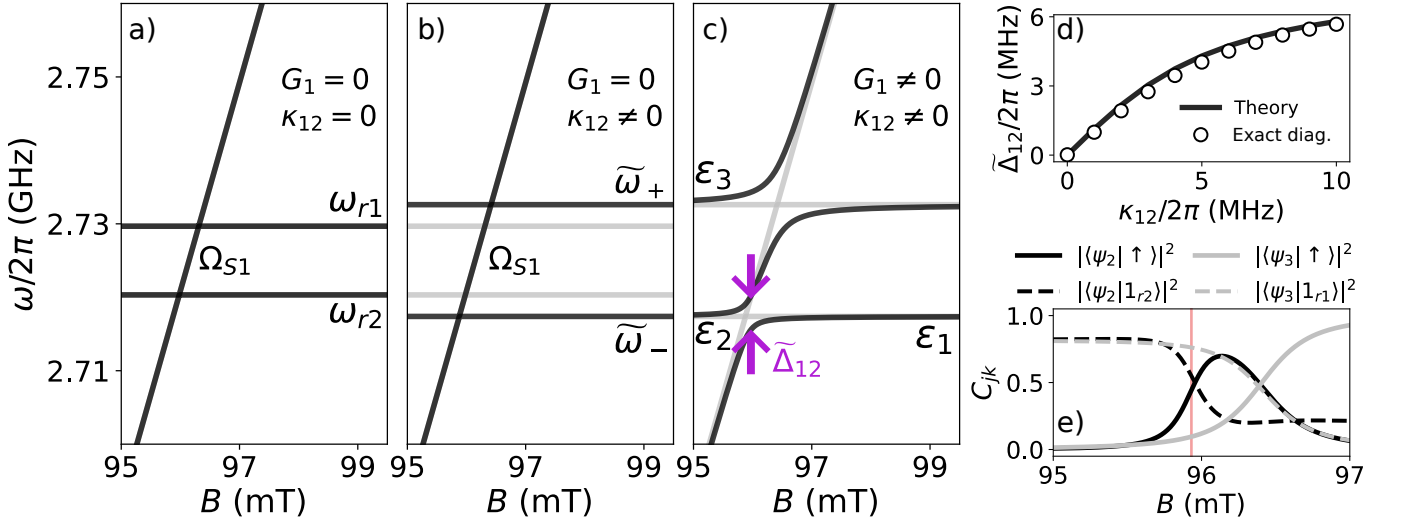


FIG. 20: Eigenvalues of the Hamiltonian (D6) that describes two coupled LERs, one of them (LER-1, in this case with the highest resonance frequency $\omega_{r,1}$) coupled to a spin ensemble. Panels a)–c) display the evolution of the system energies from the fully isolated limit to the fully interacting scenario. Light grey lines in b) and c) show the levels in a) and b), respectively, i.e. before switching a relevant interaction to better visualize its effect. Panel d) illustrates how the experimentally observed gap $\tilde{\Delta}_{1,2}$ between the two lower polariton branches depends on the inter-cavity coupling parameter $\kappa_{1,2}$. The open circles are calculated by exact diagonalization of the Hamiltonian (D6) and the solid line follows from Eqs. (D9) and (D10). Panel e) shows the probabilities of eigenstates $|\psi_2\rangle$ (with energy ϵ_2 in panel c) and $|\psi_3\rangle$ (with energy ϵ_3) in the single-excitation subspace basis for both LERs and the spin. The solid vertical red line marks the anticrossing shown by the purple arrows in panel c). The values chosen for the model parameters are $\omega_{r1}/2\pi = 2.730$ GHz, $\omega_{r2}/2\pi = 2.720$ GHz, $G_1/2\pi = 5.4$ MHz, $\kappa_{1,2}/2\pi = 6.49$ MHz.

mum spin-photon hybridization occurs when $\theta_j = \pi/2$, which corresponds to the resonance condition $\Delta_j = 0$.

In the following sections, we consider systems with increasing level of complexity, which correspond to the two experimental situations described in Section III. The first includes two coupled LERs but just one spin ensemble that interacts with only one of them. Then, we'll discuss the more general scenario where each LER hosts a different spin ensemble.

a. First scenario: one spin ensemble and 2 LERs

For clarity, we begin by studying the case where only one of the LERs hosts a coupled spin ensemble, corresponding to the setup shown in Fig. 3a. In this case, we set $\Omega_{S,2} = 0$ in Eq. (D2) and $G_2 = 0$ in Eq. (D3) and obtain the other parameters from experiment. Figure 20 shows the results of calculations that match the most salient features found in the experiments. The main finding is the remote coupling $G_{1,2}$ of the spin ensemble to the nominally empty LER, labelled in these calculations as LER-2, which is mediated by the capacitive interaction $\kappa_{1,2}$. Our aim here is to derive an expression for $G_{1,2}$ that shows how this indirect coupling depends on the circuit design (cf. Fig. 7) and then also provide information about the system energies and wave functions as a function of B .

In order to carry out these calculations and gain some intuition on the results, we'll start from the unperturbed Hamiltonian \mathcal{H}_0 [Eq. (D2)], whose energy eigenstates are trivial localized photon and spin excitations (20a), and proceed by adding the different interactions. When $\kappa_{1,2} \neq 0$ (Figs 20b and Figs 20c) it is convenient to work in a basis defined by the normal modes $\mu = +, -$ of the coupled LER pair, described by new creation and annihilation operators b_μ^\dagger and b_μ , respectively. In this new basis, the Hamiltonian reads

$$\mathcal{H} = \Omega_{S,1} S_1^z + \sum_{\mu=+,-} \tilde{\omega}_\mu b_\mu^\dagger b_\mu + \sum_{\mu=+,-} \tilde{G}_{1,\mu} (b_\mu S_1^+ + b_\mu^\dagger S_1^-), \quad (\text{D6})$$

with $\tilde{\omega}_\pm = \frac{1}{2} (\omega_{r1} + \omega_{r2} \pm \sqrt{(\Delta\omega_r)^2 + 4\kappa_{1,2}^2})$ and $\Delta\omega_r = \omega_{r2} - \omega_{r1}$. The normal mode operators b_μ and the single LER ones a_j are related by

$$b_+ = \cos \frac{\phi}{2} a_1 + \sin \frac{\phi}{2} a_2, \quad (\text{D7a})$$

$$b_- = -\sin \frac{\phi}{2} a_1 + \cos \frac{\phi}{2} a_2. \quad (\text{D7b})$$

where $\phi = \tan^{-1}(2\kappa_{1,2}/\Delta\omega_r)$ is a mixing angle that parametrizes the degree of localization of the two normal modes. Since the eigenstates $|\psi_j\rangle$ of (D6) need not be localized on either LER, from now on we'll label them in order of increasing energy (cf Fig. 20c).

It follows from Eq. (D6) that the spin ensemble, even though localized on LER-1, now couples directly to both normal modes via $\tilde{G}_{1,\pm}$. These coupling rates relate to the original G_1 as follows

$$\tilde{G}_{1,+} = G_1 \cos \frac{\phi}{2}, \quad (\text{D8a})$$

$$\tilde{G}_{1,-} = -G_1 \sin \frac{\phi}{2} \quad (\text{D8b})$$

and give rise to avoided level crossings when the spin frequency is brought into resonance to any of the normal modes, as shown in Fig. 20. The coupling $G_{1,2}$ found experimentally (Fig. 3) is then given by $\tilde{G}_{1,-}$. Using Eq. (D8) and the fact that the b_- normal mode is still predominantly localized at LER-2, we can approximate

$$G_{1,2} = \frac{G_1}{\sqrt{2}} \sqrt{1 - \frac{\Delta\omega_r}{\sqrt{(\Delta\omega_r)^2 + 4\kappa_{1,2}^2}}}, \quad (\text{D9})$$

where we have omitted the negative sign from Eq. (D8b) since it is not relevant for the discussion that follows.

The remote coupling $G_{1,2}$ then arises from the local spin-photon interaction G_1 and the delocalization of the LER pair normal modes that is generated by $\kappa_{1,2}$. When $\kappa_{1,2} \gg \Delta\omega_r$, $G_{1,2} \rightarrow G_1/\sqrt{2}$. This result is intuitive considering that, in this limit, LER excitations are fully delocalized symmetric and antisymmetric normal modes, thus the spin ensemble couples identically to both of them. As mentioned above, $G_{1,2}$ leads to the gap $\tilde{\Delta}_{1,2}$ that opens between the energies ϵ_1 and ϵ_2 of eigenstates ψ_1 and ψ_2 (Fig. 20c). To a good approximation, the relation between $G_{1,2}$ and $\tilde{\Delta}_{1,2}$ is simply given by

$$\tilde{\Delta}_{1,2} = \min(\epsilon_2 - \epsilon_1) \approx 2G_{1,2}. \quad (\text{D10})$$

This relation is fulfilled over a wide range of $\kappa_{1,2}$ values, as shown by Fig. 20d, which compares the actual gap obtained by the exact diagonalization of the full Hamiltonian (D6) to that derived from Eqs. (D9) and (D10). From a practical point of view, Eq. (D10) provides a simple method to estimate the remote coupling constant $G_{1,2}$ and, from it, $\kappa_{1,2}$ via Eq. (D9), using microwave transmission data as it is done with the data of Fig. 3.

It is also of interest to estimate the magnetic field at which the anticrossing occurs. In essence, it arises from the resonance, induced by B , between the lower polariton generated at LER-1 and the b_- mode that is closer to LER-2. Based on Hamiltonian (D6), we can restrict our analysis to the single-excitation subspace and treat the coupling $\tilde{G}_{1,-}$ as a perturbation. Consequently, we re-diagonalize the block corresponding to the symmetric photonic mode b_+ and the spin ensemble, mutually coupled via $\tilde{G}_{1,+}$ at LER-1, in order to extract its two polariton branches. The resulting polariton ‘pseudo-energies’ are then approximately given by

$$\tilde{\epsilon}_{\pm} = \frac{1}{2} \left(\Omega_{S,1} + \tilde{\omega}_+ \pm \sqrt{(\Omega_{S,1} - \tilde{\omega}_+)^2 + 4\tilde{G}_{1,+}^2} \right) \quad (\text{D11})$$

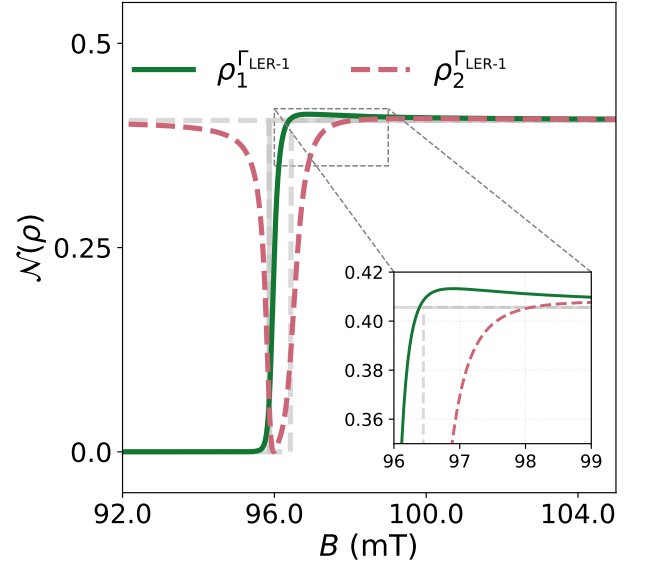


FIG. 21: Entanglement between LER-1 and LER-2 photons as a function of magnetic field. It is computed as the negativity of LER-1, defined by Eq. (D13), in eigenstates $|\psi_1\rangle$ and $|\psi_2\rangle$ of the Hamiltonian ((D6). The parameters considered are those used in Fig. 20. The light gray lines show the negativity calculated for $G_1 = 0$, i.e. when the photons are decoupled from the spins. The inset shows an zoom of the region close to the anticrossing between ψ_1 and ψ_2 in Fig. 20. A maximum entanglement between both photons then occurs for $G_1 \neq 0$ near the anticrossing between the LER-1 lower polariton and the quasi LER-2 mode b_- (see Fig. 20c).

Since $\tilde{\omega}_- < \tilde{\omega}_+$, the LER-1 polariton branch that intersects with $\tilde{\omega}_-$ is $\tilde{\epsilon}_-$. The intersection occurs when $\tilde{\epsilon}(\Omega_{S,1}) = \tilde{\omega}_-$ that leads to

$$\Omega_{S,1} = g_1 \mu_B B \approx \tilde{\omega}_- + \frac{\tilde{G}_{1,+}^2}{\tilde{\omega}_+ - \tilde{\omega}_-}, \quad (\text{D12})$$

provided that $(\Omega_{S,1} - \tilde{\omega}_+) \gg \tilde{G}_{1,+}$. The spin-photon hybridization at LER-1 then shifts the resonance field from that of the bare spin, defined by $\Omega_{S,1} = \tilde{\omega}_-$. Besides, this shift decreases as either the detuning $\Delta\omega_r$ between the two LERs or their mutual coupling $\kappa_{1,2}$ increase. This can be understood as a result of the LER-1 lower polariton branch becoming progressively closer to a pure spin excitation at its crossing with b_- , as the two modes become further apart in energy.

As a somewhat related effect, we next consider the entanglement between LER-1 and LER-2 photons in each eigenstate of the system $|\psi_j\rangle$ and how it evolves as a function of magnetic field. Here, we quantify this entanglement by using the negativity of LER-1, which is an entanglement monotone [39] and is defined as follows

$$\mathcal{N}(\rho_j) = \frac{\|\rho_j^{\Gamma_A}\|_1 - 1}{2} = \left| \sum_{\lambda_i < 0} \lambda_i \right|, \quad (\text{D13})$$

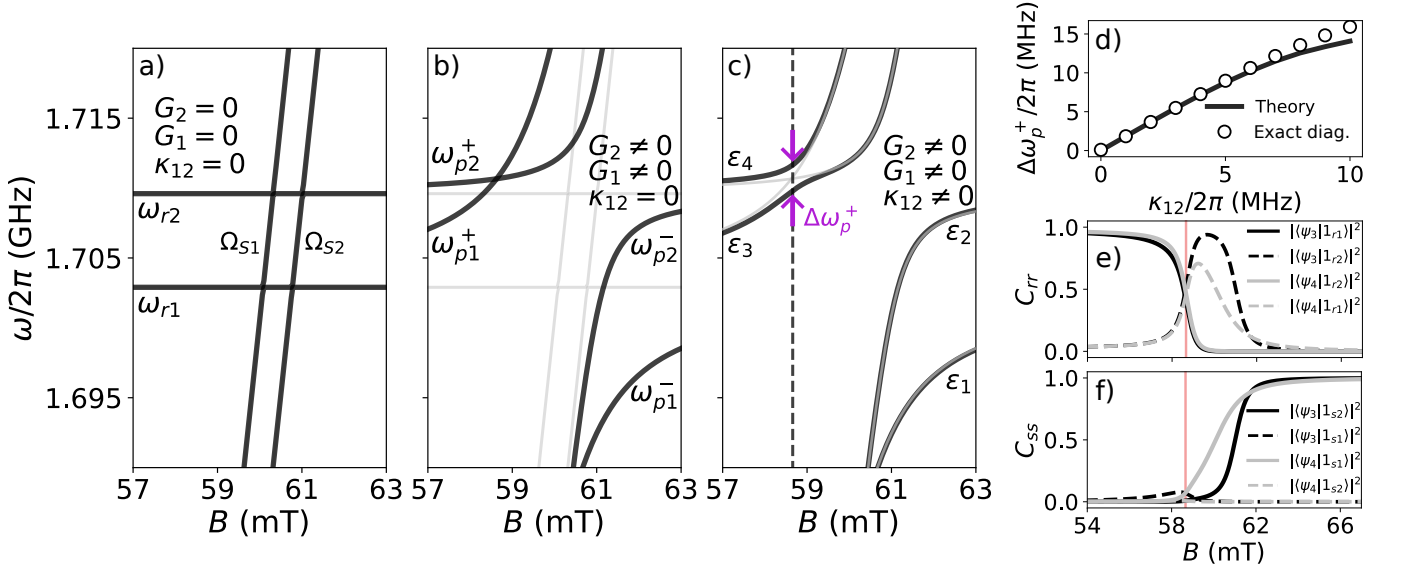


FIG. 22: Eigenvalues of the Hamiltonian (D1) that describes two coupled LERs, each of them coupled to a different spin ensemble. Panels a)–c) display the evolution of the system energies from the fully isolated limit to the fully interacting scenario (corresponding to the experimental configuration shown in Fig. 4). Panel d) illustrates the relationship between the experimentally observed gap $\Delta\omega_p^+$ between the two upper polariton branches and the inter-cavity coupling parameter $\kappa_{1,2}$. The circles are obtained by exact diagonalization of the full Hamiltonian (D1) and the solid line follows from Eqs. (D14). Finally, panels e) and f) show the probabilities of eigenstates $|\psi_3\rangle$ and $|\psi_4\rangle$ within the single-excitation subspace basis for the two LERs (panel e) and the two spin ensembles (panel f). The vertical red line indicates the anticrossing point marked by a black dashed line in panel c). The model parameters are $\omega_{r1}=1.7029$ GHz, $\omega_{r2}=1.7096$ GHz, $G_1 = 19.5$ MHz, $G_2 = 8.5$ MHz and $\kappa_{1,2} = 1.06$ MHz.

where $\rho_j^{\Gamma A} = \rho_j^{\Gamma_{\text{LER}-1}}$ is the partial transpose of the reduced density matrix ρ_j with respect to subsystem LER-1. Concurrently, such reduced density matrix is obtained by tracing out the spin (S1) degrees of freedom with respect to the subsystem defined by the two cavities, $\rho_j = \text{Tr}_{S1}(|\psi_j\rangle\langle\psi_j|)$. The λ_i elements in the right-most expression refer to the eigenvalues of $\rho_j^{\Gamma A}$.

The results, shown in Fig. 21, reveal that the hybrid character of the lower LER-1 polariton, generated by the local spin-photon coupling G_1 , leads to a local entanglement maximum near the anticrossing of this polariton with mode b_- , which is close to LER-2. As discussed above, the hybridization introduces some photonic character into the polariton branch, which then enhances the photon entanglement with respect to that given solely by $\kappa_{1,2}$ (grey lines in Fig. 21). The relative intensity of this effect diminishes as $\kappa_{1,2}$ increases, and can thus be tuned by circuit design. The higher the baseline photon entanglement, the smaller the spin contribution, provided the system is not in the regime where $G_1 \gg \kappa_{1,2}$. The experimental example considered here represents a situation dominated by a relatively large $\kappa_{1,2} \simeq 0.7\Delta\omega_r$. The next section covers a different situation in a different parameter regime.

b. Second scenario: two spin ensembles and 2 LERs

We next analyze the behavior of a system where both LERs host spin ensembles. The two ensembles possess different resonance frequencies $\Omega_{S,j}$ due to their different g -factors. Moreover, each sample presents also a different spin-photon coupling G_j to its host LER. The parameters considered here correspond to those extracted from the experiment described in Fig. 4. The main experimental phenomenon we aim to characterize is the anticrossing occurring between the two upper polariton branches.

Like in the previous case, the eigenstates and the frequencies of the two coupled hybrid spin-cavity modules have been calculated by diagonalization of Hamiltonian (D1). The results are shown in Figure 22, which again illustrates how they evolve as the different interactions are ‘switched on’. The anticrossing, characterized by the $\Delta\omega_p^+$ gap in Fig. 22c, reflects the interaction between two hybrid spin-photon excitations, each arising from one of the two spin-LER subsystems. This constitutes a generalization of the previous case, where now the capacitive photon-photon coupling $\kappa_{1,2}$ induces interactions between distant spins, alongside interactions between the spin system 1 and LER-2, and viceversa.

To understand the relationship between the gap and $\kappa_{1,2}$, we revisit the model defined by Eq. (D1), but now with $\Omega_{S,2}$ and $G_2 \neq 0$. A further distinction from the previous case is that we now proceed by first diagonalizing

the blocks corresponding to the spin-photon interaction within each LER, giving rise to polariton states $|p_j^\pm\rangle$, $j = 1, 2$, defined by Eqs. (D5a-b) with frequencies ω_p^\pm shown in Fig. 22b. Then, we treat the inter-LER coupling as a perturbation. From these, we can define the effective coupling parameter between the two upper, symmetric, polaritons as the matrix element of the perturbation \mathcal{H}_{sr} between the two states, i.e. $J_{1,2}^+ \equiv \langle p_1^+ | \mathcal{H}_{sr} | p_2^+ \rangle$.

The experimentally observed gap $\Delta\omega_p^+$ between the frequencies of these polariton branches can then be approximated by

$$\Delta\omega_p^+ \simeq 2J_{1,2}^+ = 2\kappa_{1,2} \cos \frac{\theta_1}{2} \cos \frac{\theta_2}{2}. \quad (\text{D14})$$

The gap scales as $\kappa_{1,2}$, reflecting the dominant photonic nature of the polaritons, but depends also on their spin components, defined by θ_1 and θ_2 , which are induced by the local spin-photon interactions G_1 and G_2 . In fact, it is their spin component that renders them sensitive to the magnetic field and ultimately drives the crossing. Note that $J_{1,2}^+$ is not purely proportional to $\kappa_{1,2}$, as can be seen in Fig. 22d, since $\kappa_{1,2}$ also determines the magnetic field at which the two polariton branches cross. In this case, the approximation breaks down earlier than for Eq. (D10) due to the presence of additional interacting subsystems with non-negligible couplings.

The combination of local and remote interactions leads to correlations between the spin and photon components, which are tuned by the magnetic field as it brings local polaritons in and out mutual resonance. This effect can be seen by looking at the probabilities that the exact eigenstates $|\psi_3\rangle$ and $|\psi_4\rangle$ (again sorted by energy) have in the basis of local single photon and single spin excitations. These probabilities are shown in panels e) and f) of Fig. 22, respectively. The vertical red line corresponds to the anticrossing marked as a dashed black line in panel c). At this point, the two wavefunctions become maximally delocalized over the two LER photons. The different spin-photon couplings at each LER lead to asymmetric correlations between their photon excitations. For instance, panel e) shows that the mode originating as LER-1 acquires significantly more LER-2 character than the converse. Interestingly, the mode originating as LER-2 exhibits less hybridization with LER-1 because it simultaneously transitions into a ‘spin-1’ excitation. Here, the level crossings do not merely involve a predominantly photon-like eigenstate transitioning into a spin-like excitation, as in a conventional polariton. Rather, an eigenstate starting as a LER- j photon converts after the crossing into an excitation of the spin ensemble i located at the other LER- i . At the intermediate point, the wavefunctions exhibit non-zero amplitudes for all four subsystems.

To better understand this behavior and quantify the effective spin-spin interaction mediated by the circuit, we move to a different basis to that used in Eqs. (D5)a-d. Specifically, we return to the photonic normal mode basis [cf. Eq. (D6)] and treat the spin-mode coupling as a

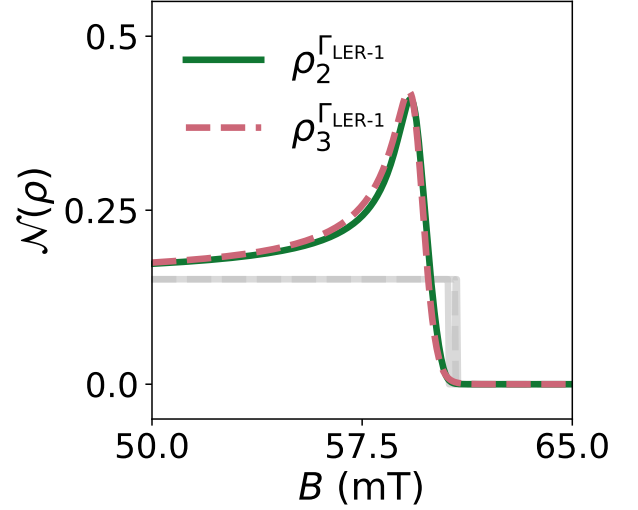


FIG. 23: Photon entanglement as a function of the external magnetic field computed as the negativity for the subsystem LER-1 according to Eq. (D13), after tracing out the spin degrees of freedom for subsystems s1 and s2. The parameters considered are the same as in Fig. 22. The gray lines indicate the negativity evolution for the same eigenstates as the respective colored lines but in the scenario where $G_1 = G_2 = 0$.

perturbation. Then, we now define

$$\mathcal{H}'_0 = \sum_j \Omega_{S_j} S_j^z + \sum_{\mu=+,-} \tilde{\omega}_\mu b_\mu^\dagger b_\mu \quad (\text{D15})$$

and

$$\tilde{V} = \sum_{j,\mu} \tilde{G}_{j,\mu} (b_\mu S_j^+ + b_\mu^\dagger S_j^-), \quad (\text{D16})$$

where the normal mode operators b_\pm have been defined in Eqs. (D7)a-b, their couplings to spin-1 $\tilde{G}_{1,\pm}$ are those defined in Eqs. (D8)a-b and their couplings to spin-2 read

$$\tilde{G}_{2,+} = G_2 \sin \frac{\phi}{2}, \quad (\text{D17a})$$

$$\tilde{G}_{2,-} = G_2 \cos \frac{\phi}{2}. \quad (\text{D17b})$$

From here, it is possible to derive an effective Hamiltonian by applying a Schrieffer-Wolff transformation, defined by $\mathcal{H}_{\text{eff}} = e^{\mathcal{S}} \mathcal{H} e^{-\mathcal{S}}$ [40]. The operator \mathcal{S} is such that the relation $\tilde{V} + [\mathcal{S}, \mathcal{H}'_0] = 0$ is fulfilled. After this transformation, the effective Hamiltonian reads

$$\mathcal{H}_{\text{eff}} = \mathcal{H}'_0 + \frac{1}{2} [\mathcal{S}, \tilde{V}] + \frac{1}{3} [\mathcal{S}, [\mathcal{S}, \tilde{V}]] + \dots \quad (\text{D18})$$

For the present case, the anti-hermitian operator \mathcal{S} reads

$$\mathcal{S} = \sum_{j,\mu} \frac{\tilde{G}_{j,\mu}}{\Delta_{j,\mu}} (b_\mu S_j^+ - b_\mu^\dagger S_j^-), \quad (\text{D19})$$

with $\tilde{\Delta}_{j,\mu} = \Omega_{S,j} - \tilde{\omega}_\mu$. In the resulting effective Hamiltonian, we are going to eliminate, up to first order in the series (D18), the interaction between the spins and the normal modes. This approximation will properly describe the system whenever $G_j \ll \tilde{\Delta}_{j,\mu}$, i.e. in the dispersive regime. If we stop the series (D18) at the second order, the effective Hamiltonian takes the form

$$\mathcal{H}_{\text{eff}} = \mathcal{H}'_0 + \mathcal{H}_{\text{disp}} + \mathcal{H}_{\text{spin-spin}}. \quad (\text{D20})$$

The first term, \mathcal{H}'_0 , is just Eq.(D15), the second one,

$$\mathcal{H}_{\text{disp}} = \sum_{j,\mu} \frac{\tilde{G}_{j,\mu}^2}{\tilde{\Delta}_{j,\mu}} (2b_\mu^\dagger b_\mu + 1) S_j^z, \quad (\text{D21})$$

describes the usual dispersive effect of the spin-normal mode couplings on the frequencies of both, and the third and last term,

$$\mathcal{H}_{\text{spin-spin}} = \frac{J}{2} (S_1^+ S_2^- + S_1^- S_2^+), \quad (\text{D22})$$

where $J = \sum_\mu \tilde{G}_{1,\mu} \tilde{G}_{2,\mu} (\tilde{\Delta}_{1\mu}^{-1} + \tilde{\Delta}_{2\mu}^{-1})$, describes an emerging spin-spin interaction. Note that $J \propto G_1 G_2 \kappa_{1,2}$ since it is a third-order process. The spin ensemble j first couples to its host LER- j , via G_j , which in turn forms a hybrid mode with the adjacent resonator through $\kappa_{1,2}$, and then interacts with the distant spin ensemble, i , via G_i . It is important to emphasize that this analysis holds only in the dispersive regime where $G_j \ll \tilde{\Delta}_{j,\mu}$. To study the spin and photon hybridization near resonance, it is necessary to resort to the numerical diagonalization methods illustrated in Fig. 22.

Finally, we revisit the evolution of photon entanglement between the two cavities as a function of magnetic field, now in the presence of two spin ensembles. Applying the same analysis as in the previous scenario, Fig. 23

shows that this entanglement, quantified by the negativity defined in Eq. (D13), is enhanced even further by the presence of the spins as compared to the baseline entanglement of the same cavities in the absence of spins. Once again, the spin ensembles act as local ‘tuning knobs’ of the polariton frequencies, bringing them into resonance via their interaction with the magnetic field.

The results discussed in this and the previous section illustrate the possibilities that this hybrid polariton platform offers for controlling spin-spin and photon-photon correlations within a chip by playing with the magnetic field and other external parameters. Besides, the margins over which effective spin-spin interactions as well as photon entanglement can be varied are determined by the circuit design. Last but not least, this theoretical framework provides a solid basis to interpret the microwave transmission experiments reported in previous sections. The methods are described in the following.

2. Input-output theory: calculation of microwave transmission

To corroborate the theoretical arguments developed in this section so far, we resort to experimental validation. In this work, such validation is provided by microwave transmission experiments, in which photons sent through a waveguide interact with the system, yielding direct information about its energy level spectrum. To describe these experiments, we employ standard input-output theory [41]. Starting from the Hamiltonian introduced in Eqs. (D1-D4), we map our spins onto harmonic oscillators via the Holstein-Primakoff transformation [42]. Then, each spin ensemble is characterized by its creation and annihilation operators, c_j^\dagger and c_j , respectively. Solving for the time evolution of the expectation values of operators a_j , a_j^\dagger , c_j , and c_j^\dagger by applying standard approximations, such as the rotating wave approximation, and focusing on the steady-state solution for a perturbative driving of amplitude α_{in} , we arrive at

$$-i\alpha_{\text{in}} \begin{pmatrix} \sqrt{\gamma_{c1}} \\ \sqrt{\kappa_{c1}} \\ \sqrt{\kappa_{c2}} \\ \sqrt{\gamma_{c2}} \end{pmatrix} = \underbrace{\begin{pmatrix} i(\Omega_{S1} - \omega) + \gamma_1 & iG_1 & 0 & 0 \\ iG_1 & i(\omega_{r1} - \omega) + \kappa_1 & i\kappa_{1,2} & 0 \\ 0 & i\kappa_{1,2} & i(\omega_{r2} - \omega) + \kappa_2 & iG_2 \\ 0 & 0 & iG_2 & i(\Omega_{S2} - \omega) + \gamma_2 \end{pmatrix}}_{\hat{C}} \begin{pmatrix} \langle c_1 \rangle \\ \langle a_1 \rangle \\ \langle a_2 \rangle \\ \langle c_2 \rangle \end{pmatrix}, \quad (\text{D23})$$

where κ_j is the overall photon decay rate for $\langle a_j \rangle$ in each LER, $\kappa_{c,j}$ the coupling rate of each LER to the readout transmission line, γ_j the total loss rate for each molecular spin, and $\gamma_{c,j}$ accounts for the direct coupling between the spins and the transmission line.

For the present analysis, we neglect the coupling between the spin ensembles and the transmission line (i.e., we make $\gamma_{c,j} = 0$), as the contact between the deposited

sample and the line is usually minimal. This simplification enables us to derive an analytical expression for the transmission based on the response of each resonator to the driving field, which is given by

$$S_{21} = 1 - \left(\frac{\sqrt{\kappa_{c1}} i \langle a_1 \rangle}{\alpha_{\text{in}}} + \frac{\sqrt{\kappa_{c2}} i \langle a_2 \rangle}{\alpha_{\text{in}}} \right). \quad (\text{D24})$$

Now $\langle a_1 \rangle$ and $\langle a_2 \rangle$ can be obtained analytically, by inverting the 4×4 matrix on the right-hand side of Eq. (D23).

$$\frac{i\langle a_1 \rangle}{\alpha_{in}} = \left[\widehat{C}^{-1} \begin{pmatrix} 0 \\ \sqrt{\kappa_{c1}} \\ \sqrt{\kappa_{c2}} \\ 0 \end{pmatrix} \right]_2 = (\widehat{C}^{-1})_{2,2}\sqrt{\kappa_{c1}} + (\widehat{C}^{-1})_{2,3}\sqrt{\kappa_{c2}} \quad (\text{D25})$$

$$\frac{i\langle a_2 \rangle}{\alpha_{in}} = \left[\widehat{C}^{-1} \begin{pmatrix} 0 \\ \sqrt{\kappa_{c1}} \\ \sqrt{\kappa_{c2}} \\ 0 \end{pmatrix} \right]_3 = (\widehat{C}^{-1})_{3,2}\sqrt{\kappa_{c1}} + (\widehat{C}^{-1})_{3,3}\sqrt{\kappa_{c2}}, \quad (\text{D26})$$

where we have denoted $[\cdot]_m$ the m th component of the corresponding column vector. Thus, we see that we only need four of the matrix elements of \widehat{C}^{-1} (three actually, as \widehat{C} is symmetric).

In order to get those matrix elements, we write our 3-diagonal symmetric matrix \widehat{C} compactly as follows:

$$\widehat{C} = \begin{pmatrix} u_1 & v_1 & 0 & 0 \\ v_1 & u_2 & v_2 & 0 \\ 0 & v_2 & u_3 & v_3 \\ 0 & 0 & v_3 & u_4 \end{pmatrix}. \quad (\text{D27})$$

We can get the required matrix elements of \widehat{C}^{-1} from the corresponding minors of \widehat{C} by the formula $(\widehat{C}^{-1})_{j,k} = (-1)^{j+k} M_{k,j} / \det \widehat{C}$. Here the minor $M_{j,k}$ is the determinant of the submatrix obtained by deleting the j th row and the k th column of \widehat{C} .

$$\begin{aligned} \begin{vmatrix} u_1 & v_1 & 0 & 0 \\ v_1 & u_2 & v_2 & 0 \\ 0 & v_2 & u_3 & v_3 \\ 0 & 0 & v_3 & u_4 \end{vmatrix} &= u_1 \begin{vmatrix} u_2 & v_2 & 0 \\ v_2 & u_3 & v_3 \\ 0 & v_3 & u_4 \end{vmatrix} - v_1 \begin{vmatrix} v_1 & 0 & 0 \\ v_2 & u_3 & v_3 \\ 0 & v_3 & u_4 \end{vmatrix} \\ &= u_1 [u_2 \underbrace{(u_3 u_4 - v_3^2)}_{\theta_2} - u_4 v_2^2] - v_1^2 \underbrace{(u_3 u_4 - v_3^2)}_{\theta_2} \\ &= \underbrace{(u_1 u_2 - v_1^2)}_{\theta_1} \theta_2 - u_1 u_4 v_2^2, \end{aligned}$$

as announced.

Let us now plug the above \widehat{C}^{-1} matrix elements in

Denoting that matrix by \widehat{C} , and applying \widehat{C}^{-1} to both sides of Eq. (D23), we have (recall we set $\gamma_{c1} = \gamma_{c2} = 0$)

All determinants involved can be written in terms of the following two combinations

$$\begin{aligned} \theta_1 &= u_1 u_2 - v_1^2 \\ \theta_2 &= u_3 u_4 - v_3^2, \end{aligned}$$

which are the determinants of the 2×2 diagonal boxes in which the matrix can be partitioned. Indeed, $\det \widehat{C} = \theta_1 \theta_2 - u_1 u_4 v_2^2$, while

$$\begin{aligned} (\widehat{C}^{-1})_{2,2} &= u_1 \theta_2 / \det \widehat{C} \\ (\widehat{C}^{-1})_{3,3} &= u_4 \theta_1 / \det \widehat{C} \\ (\widehat{C}^{-1})_{2,3} &= (\widehat{C}^{-1})_{3,2} = -(u_1 u_4) v_2 / \det \widehat{C}. \end{aligned}$$

The last two are duly equal, since \widehat{C}^{-1} ought to be symmetric too. The 3×3 minors employed come out readily, as the matrix has many zeroes. As for $\det \widehat{C}$, it follows by Laplace expansion as:

the right-hand side of Eqs. (D25) and (D26) and then assemble the term in the parenthesis of Eq. (D24). The result reads

$$\sqrt{\kappa_{c1}} \frac{i\langle a_1 \rangle}{\alpha_{in}} + \sqrt{\kappa_{c2}} \frac{i\langle a_2 \rangle}{\alpha_{in}} = \frac{\kappa_{c1} u_1 \theta_2 + \kappa_{c2} u_4 \theta_1 - 2\sqrt{\kappa_{c1} \kappa_{c2}} (u_1 u_4) v_2}{\theta_1 \theta_2 - (u_1 u_4) v_2^2},$$

and we are almost done. We divide numerator and denominator by $u_1 u_4$, introduce $z_1 \equiv \theta_1/u_1 = u_2 - v_1^2/u_1$ and $z_2 \equiv \theta_2/u_4 = u_3 - v_3^2/u_4$, so we can write

$$S_{21} = 1 - \frac{\kappa_{c1} z_2(\omega) + \kappa_{c2} z_1(\omega) - 2i\sqrt{\kappa_{c1}\kappa_{c2}} \kappa_{1,2}}{z_1(\omega)z_2(\omega) + \kappa_{1,2}^2}. \quad (\text{D28})$$

Here we reverted to the original $-v_1^2 = G_1^2$ and $-v_3^2 = G_2^2$, along with $v_2 = i\kappa_{1,2}$. We close with explicit expressions for the important functions z_1 and z_2 . They can be written in an unified way as ($j = 1, 2$)

$$z_j(\omega) = [i(\omega_{rj} - \omega) + \kappa_j] + \frac{G_j^2}{[i(\Omega_{Sj} - \omega) + \gamma_j]}. \quad (\text{D29})$$

The terms in the square brackets are u_2 & u_1 , for $j = 1$, and u_3 & u_4 , when $j = 2$, as given in the original matrix. Equipped with these expressions, we can extract the values of the parameters defining our model from the experimental measurements.

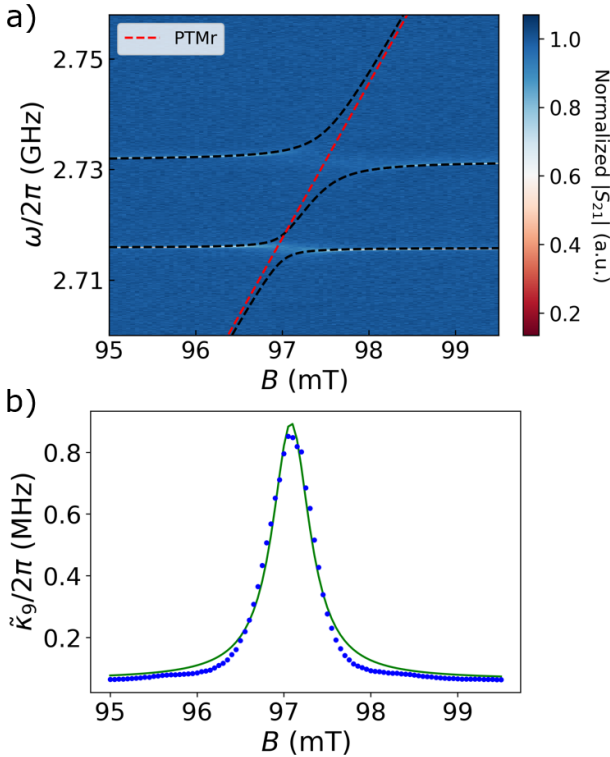


FIG. 24: a) Result of fitting the eigenvalues of the Hamiltonian (D6) to the experimental modes determined from microwave transmission data for LER-9 and LER-10 (cf Fig. 3). LER-9 remains empty while LER-10 hosts a PTMr sample, whose resonance frequency is shown as a red dotted line, leading to a local spin-photon collective coupling $G_{10}/2\pi = 5.4$ MHz. b) Effective half width at half maximum of LER-9 as a function of magnetic field (dots) and least-squares fit based on Eq. (D30), yielding $G_{9,10}/2\pi = 2.46$ MHz.

3. Application

a. One spin ensemble scenario: microwave transmission and remote spin-photon coupling

Analogous to the theoretical framework developed previously, we begin by examining the case where only one LER within a pair couples to a spin ensemble, while the other remains empty. This scenario corresponds to the experiments performed with LER-9 and LER-10, shown in Fig. 3. Microwave transmission results obtained for this system are shown in Fig. 24, which show an effective coupling of the spin ensemble to both modes.

In order to extract the effective coupling constants, we adopt the following strategy. First, we treat the spin-free LER-9 as if it were a standard LER coupled to a spin ensemble with a characteristic coupling constant given by $G_{9,10}$. Using input-output theory in the weak coupling regime [21], we fit the magnetic field dependence of this LER effective line width $\tilde{\kappa}_9$ with the expression:

$$\tilde{\kappa}_9 = \kappa_9 + \left[\frac{G_{9,10}^2}{(\Omega_S - \tilde{\omega}_r)^2 + \gamma^2} \right] \gamma. \quad (\text{D30})$$

The result is shown in Fig. 24b. The fit allows estimating $G_{9,10}$, as well as the spin resonance linewidth γ .

Note that, as discussed in Appendix D 1 a above, the resonance does not occur when the polariton frequency crosses $\omega_{r,9}$ but rather $\tilde{\omega}_-$. Consequently, in Eq. (D30), $\tilde{\omega}_r = \tilde{\omega}_-$. Based on the relationship between $\omega_{r,j}$ and $\tilde{\omega}_\pm$ [cf. Eq. (D6)] along with Eq. (D9) for the remote coupling $G_{9,10}$, we can determine the bare resonance frequencies of each LER and $\kappa_{1,2}$. We find $\kappa_{1,2}/2\pi = 6.49$ MHz, $\omega_{r,1}/2\pi = 2.730$ GHz, $\omega_{r,2}/2\pi = 2.720$ GHz, $\gamma/2\pi = 7.3$ MHz. The fits are shown in Fig. 24. It is worth mentioning that without the presence of the spin ensemble in this experiment, determining the cavity parameters $\omega_{r,j}$ and $\kappa_{1,2}$ would have been impossible. Since the transmission experiment probes the coupled normal modes, we would face an underdetermined system of equations, because distinct sets of values for the detuning between bare resonance frequencies and the inter-resonator coupling can yield the same level splitting. In this scenario, the spin serves to fully characterize the coupled photonic system.

In order to validate this procedure, we perform simulations of the microwave transmission with Eq. (D28) and with all parameters, save for $\kappa_{1,2}$, as given above. By varying $\kappa_{1,2}$, we have checked that the remote coupling $G_{9,10}$ derived from the fits of microwave transmission based on Eq. (D30), follows the expected trend, predicted by (D9). The results, displayed in Fig. 25, confirm that the analysis of the experimental results in Fig. 24 do indeed provide a $G_{9,10}$ value consistent with theory.

Finally, we also test the prediction of Eq. (D12) for the crossing magnetic field between the polariton formed at the LER that hosts a spin ensemble and the normal mode that is closest to the other LER. We consider a

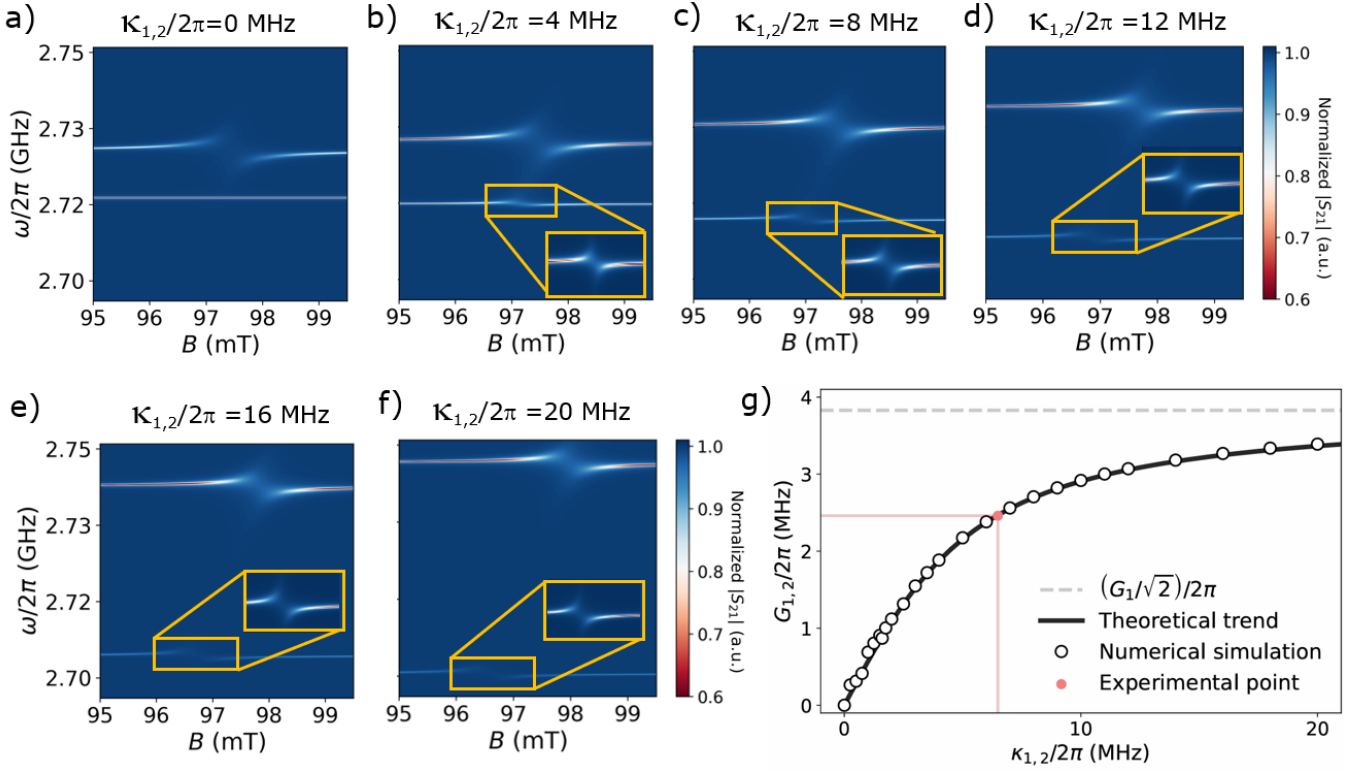


FIG. 25: a)-f) 2D microwave transmission maps simulated, using Eq. (D28), for a coupled LER-1 and LER-2 pair with different values of $\kappa_{1,2}$, as indicated. Other relevant parameters are close to those estimated for LER-9 and LER-10, shown in Fig. 3. The lowest frequency LER-1 remains empty while LER-2 couples to a spin ensemble with $G_2/2\pi = 5.4$ MHz. As $\kappa_{1,2}$ increases, the avoided level crossing observed for LER-1 widens. g) Remote coupling of the spin ensemble to LER-1, $G_{1,2}$, determined by fitting the LER-1 resonance with $|S_{21}| = |1 - \frac{\kappa_{c,1}}{z_1(\omega)}|$, where $z_1(\omega) = i(\omega_{r,1} - \omega) + \kappa + \frac{G_{1,2}^2}{i(\Omega_{S,2} - \omega) + \gamma_2}$ [cf Eq. (D29)]. The solid line follows the prediction given by Eq. (D9). The orange solid dot is the experimental $G_{9,10}$ coupling constant, which allows determining $\kappa_{1,2}$.

LER pair formed by LER-1, strongly coupled to a spin ensemble, and the empty LER-2. Figure 26 shows microwave transmission maps calculated for different values of $\kappa_{1,2}$. In this figure, a yellow star marks the crossing predicted from Eq. (D12), which agrees very well with the simulation. These simulations also confirm that the crossing approaches the bare spin resonance (indicated by a yellow dashed line) as $\kappa_{1,2}$ increases.

b. *Two spin ensemble scenario: eigenstates, microwave transmission and polariton visibilities*

We now turn to the case involving two distinct spin ensembles, each coupled to a separate LER. Similarly to the previous case, we can extract the relevant parameters in Eq. (D1) by fitting the experimental transmission data. In this way, we are able to determine the local spin-photon couplings ($G_1/2\pi = 19.5$ MHz, and $G_2/2\pi = 8.5$ MHz), the inter-cavity coupling ($\kappa_{1,2}/2\pi = 1.06$ MHz), and the bare LER frequencies ($\omega_{r,1}/2\pi = 1.7029$ GHz and $\omega_{r,2}/2\pi = 1.7096$ GHz). Fig-

ure 27 shows that the system eigenfrequencies obtained by the exact diagonalization of the Hamiltonian reproduce the experimental modes.

There is, however, an interesting detail concerning the experimental visibilities of some of these modes. Figure 4f shows that one of the two polariton branches becomes darker, while the other one becomes brighter near their avoided crossing. Yet, none of them vanishes. This seems at odds with the theoretical predictions derived from Eq. (D28) for this system. If one examines the wave functions obtained numerically for this model, it is observed that the $|\psi_3\rangle$ eigenstate becomes an antisymmetric combination of LER-1 and LER-2 photons near the anticrossing (Figs. 22c and 22e). According to Eq. (D24), at the point where this perfectly antisymmetric superposition occurs null visibility is expected. That is, the normalized transmission should reach unity at that point, as we are dealing with a dark state. The non-zero visibility observed experimentally calls for some asymmetry in the coupling of both LERs to the readout line.

In order to account for this effect, it is necessary to include in the model a direct coupling between the two

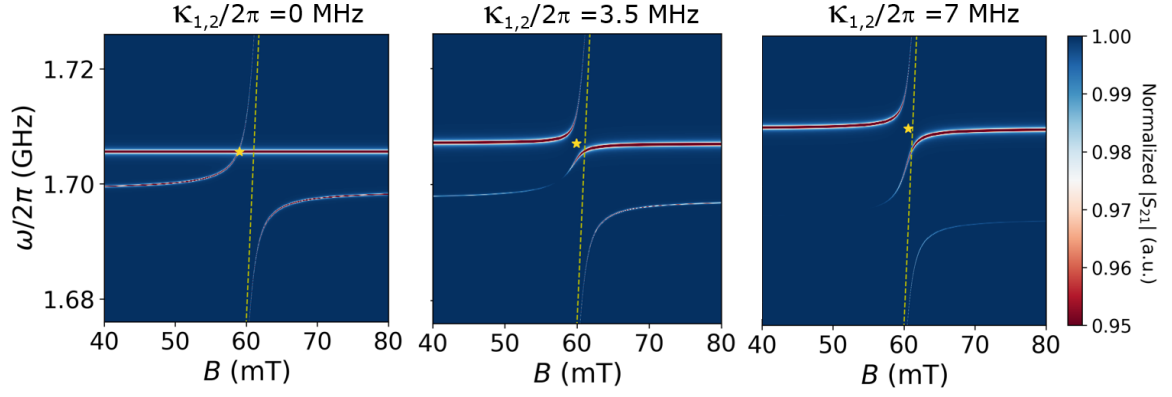


FIG. 26: Simulation of the transmission signal for a LER pair coupled to one spin ensemble and for different values of $\kappa_{1,2}$. The lower frequency LER-1 hosts a molecular sample leading to a local $G_1/2\pi \approx 20$ MHz and LER-2 is empty. The yellow dotted line denotes the bare $\Omega_{S,1}$ as a function of magnetic field. The anti-crossing occurs at the magnetic field where the frequency of the polariton mode formed at LER-1, not $\Omega_{S,1}$, crosses the frequency of the other normal mode, as predicted by (D12) that is marked by a star.

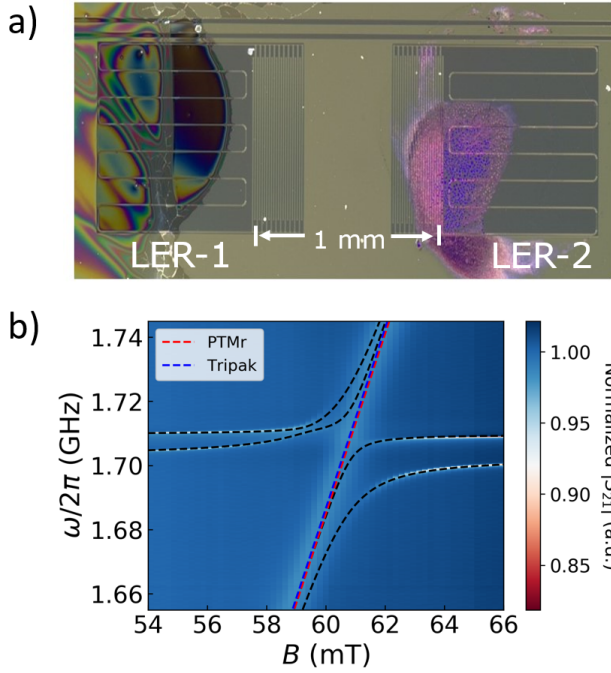


FIG. 27: a) Optical microscopy image of the two coupled LER-1 and LER-2, hosting $N \sim 5 \times 10^{14}$ PTMr and Tripak⁻ free radical molecules, respectively. b) 2D microwave transmission map measured near their resonance frequencies at $T = 11$ mK and as a function of magnetic field. The lines show the eigenfrequencies obtained by exact diagonalization of the Hamiltonian (D1) using the parameter values derived by fitting the experimental transmission with Eq. (D28). We find $\omega_{r,1}/2\pi = 1.703$ GHz, $\omega_{r,2}/2\pi = 1.710$ GHz, $G_1/2\pi = 19.5$ MHz, $G_2/2\pi = 8.5$ MHz and $\kappa_{1,2}/2\pi = 1.06$ MHz.

spin ensembles and the readout waveguide, represented in in Eq. (D23) by the parameters $\gamma_{c,j}$. Furthermore, given

the microscopic geometry of the system (see Fig. 28a), we treat this coupling as a complex number. This additional phase accounts for the fact that spins within the ensemble do not all experience the same microwave magnetic field, differing not only in magnitude (due to varying proximity to the inductor lines) but also in phase (as this particular resonator design exhibits non-zero field components in all spatial directions). Figure 28 shows that simply treating $\gamma_{c,j}$ as a non-zero real value is insufficient; rather, the phase θ modifies the visibility of the polariton branch of interest. Given the experimental situation, we take $\gamma_{c,1} = \lambda e^{i\theta}$ with $\lambda/2\pi = 65$ kHz and $\gamma_{c,2} = 0$. This change in Eq. (D23) forces us to resort to numerical analysis to compute the response for the operators and hence the microwave transmission, which now takes the form

$$S_{21} = 1 - \sqrt{\kappa_{c,1}} \frac{i\langle a_1 \rangle}{\alpha_{\text{in}}} - \sqrt{\kappa_{c,2}} \frac{i\langle a_2 \rangle}{\alpha_{\text{in}}} - \sqrt{\gamma_{c1}} \frac{i\langle c_1 \rangle}{\alpha_{\text{in}}}. \quad (\text{D31})$$

By taking into account this effect, we are able to qualitatively reproduce the signal shown in Fig. 4. A more refined fit would require accounting for the specific field distribution and orientations derived from the microscopic model.

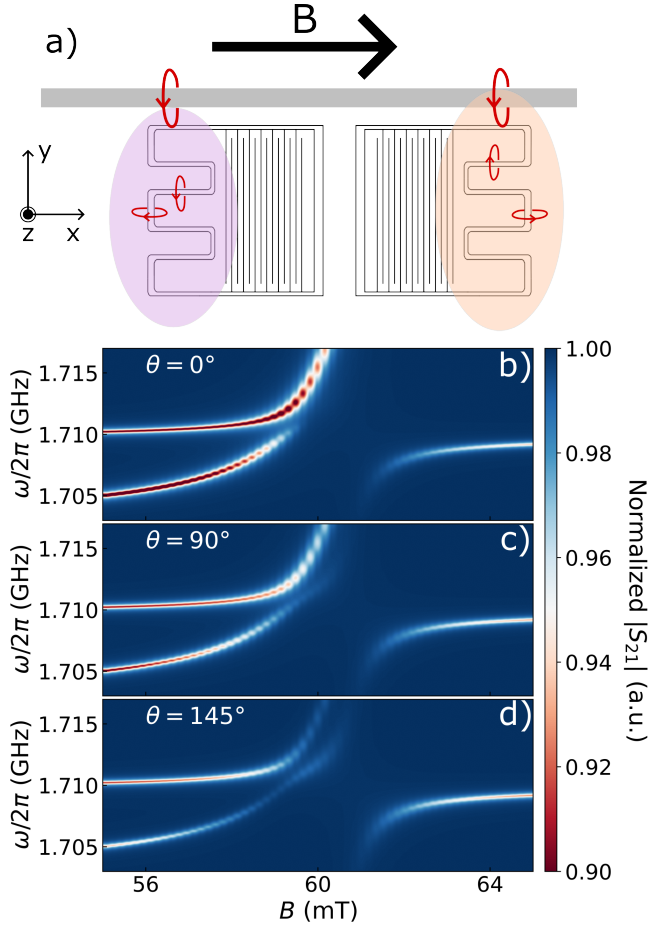


FIG. 28: a) Sketch of the LER-1 and LER-2 pair, showing the coupling of the Tripak⁻ (purple) and PTMr (orange) molecular spin ensembles to each LER and to the readout transmission line (in grey at the top). b-d) Dependence of microwave transmission visibility on the effective relative angle between the microwave field generated by the transmission line and the field generated by the LER inductor. The microwave 2D map in panel d) corresponds to the final fit shown in Fig. 5c

-
- [1] A. Blais, R.-S. Huang, A. Wallraff, S. M. Girvin, and R. J. Schoelkopf, *Phys. Rev. A* **69**, 062320 (2004).
- [2] A. Blais, A. L. Grimsmo, S. M. Girvin, and A. Wallraff, *Rev. Mod. Phys.* **93**, 025005 (2021).
- [3] A. Wallraff, D. I. Schuster, A. Blais, L. Frunzio, R.-S. Huang, J. Majer, S. Kumar, S. M. Girvin, and R. J. Schoelkopf, *Nature* **431**, 162 (2004).
- [4] T. Niemczyk, F. Deppe, H. Huebl, E. P. Menzel, F. Hocke, M. J. Schwarz, J. J. García-Ripoll, D. Zueco, T. Hümmer, E. Solano, M. A., and G. R., *Nature Physics* **6**, 772 (2010).
- [5] A. Wallraff, D. I. Schuster, A. Blais, L. Frunzio, J. Majer, M. H. Devoret, S. M. Girvin, and R. J. Schoelkopf, *Phys. Rev. Lett.* **95**, 060501 (2005).
- [6] A. A. Houck, D. I. Schuster, J. M. Gambetta, J. A. Schreier, B. R. Johnson, J. M. Chow, L. Frunzio, J. Majer, M. H. Devoret, S. M. Girvin, and R. J. Schoelkopf, *Nature* **449**, 328 (2007).
- [7] C. Bonizzoni, A. Ghirri, F. Santanni, and M. Affronte, *NPJ Quantum Information* **10**, 41 (2024).
- [8] J. Majer, J. M. Chow, J. M. Gambetta, J. Koch, B. R. Johnson, J. A. Schreier, L. Frunzio, D. I. Schuster, A. A. Houck, A. Wallraff, A. Blais, M. H. Devoret, S. M. Girvin, and R. J. Schoelkopf, *Nature* **449**, 443 (2007).

- [9] F. Borjans, X. G. Croot, X. Mi, M. J. Gullans, and J. R. Petta, *Nature* **577**, 195 (2020).
- [10] P. Harvey-Collard, J. Dijkema, G. Zheng, A. Sammak, G. Scappucci, and L. M. K. Vandersypen, *Phys. Rev. X* **12**, 021026 (2022).
- [11] J. Dijkema, X. Xue, P. Harvey-Collard, M. Rimbach-Russ, S. L. de Snoo, G. Zheng, A. Sammak, G. Scappucci, and L. M. K. Vandersypen, *Nature Physics* **21**, 168 (2025).
- [12] R. H. Dicke, *Phys. Rev.* **93**, 99 (1954).
- [13] D. I. Schuster, A. P. Sears, E. Ginossar, L. DiCarlo, L. Frunzio, J. J. L. Morton, H. Wu, G. A. D. Briggs, B. B. Buckley, D. D. Awschalom, and R. J. Schoelkopf, *Phys. Rev. Lett.* **105**, 140501 (2010).
- [14] Y. Kubo, F. R. Ong, P. Bertet, D. Vion, V. Jacques, D. Zheng, A. Dréau, J.-F. Roch, A. Auffeves, F. Jelezko, J. Wrachtrup, M. F. Barthe, P. Bergonzo, and D. Esteve, *Phys. Rev. Lett.* **105**, 140502 (2010).
- [15] H. Wu, R. E. George, J. H. Wesenberg, K. Mølmer, D. I. Schuster, R. J. Schoelkopf, K. M. Itoh, A. Ardavan, J. J. L. Morton, and G. A. D. Briggs, *Phys. Rev. Lett.* **105**, 140503 (2010).
- [16] R. Amsüss, C. Koller, T. Nöbauer, S. Putz, S. Rotter, K. Sandner, S. Schneider, M. Schramböck, G. Steinhäuser, H. Ritsch, J. Schmiedmayer, and J. Majer, *Phys. Rev. Lett.* **107**, 060502 (2011).
- [17] A. Ghirri, C. Bonizzoni, D. Gerace, S. Sanna, A. Cassinese, and M. Affronte, *Applied Physics Letters* **106**, 184101 (2015).
- [18] C. Bonizzoni, A. Ghirri, M. Atzori, L. Sorace, R. Sessoli, and A. Affronte, *Scientific Reports* **7**, 13096 (2017).
- [19] M. Mergenthaler, J. Liu, J. J. Le Roy, N. Ares, A. L. Thompson, L. Bogani, F. Luis, S. J. Blundell, T. Lancaster, A. Ardavan, G. A. D. Briggs, P. J. Leek, and E. A. Laird, *Phys. Rev. Lett.* **119**, 147701 (2017).
- [20] S. Lenz, D. König, D. Hunger, and J. van Slageren, *Advanced Materials* **33**, 2101673 (2021).
- [21] V. Rollano, M. C. de Ory, C. D. Buch, M. Rubín-Osanz, D. Zueco, C. Sánchez-Azqueta, A. Chiesa, D. Granados, S. Carretta, A. Gomez, S. Piligkos, and F. Luis, *Communications Physics* **5**, 246 (2022).
- [22] A. Ghirri, C. Bonizzoni, F. Troiani, N. Buccheri, L. Beverina, A. Cassinese, and M. Affronte, *Phys. Rev. A* **93**, 063855 (2016).
- [23] T. Astner, S. Nevlacsil, N. Peterschofsky, A. Angerer, S. Rotter, S. Putz, J. Schmiedmayer, and J. Majer, *Phys. Rev. Lett.* **118**, 140502 (2017).
- [24] A. Chiesa, P. Santini, D. Gerace, J. Raftery, H. A. A., and S. Carretta, *Sci. Reports* **5**, 16036 (2005).
- [25] S. Roca-Jerat, E. Macaluso, A. Chiesa, P. Santini, and S. Carretta, *Mater. Horiz.* **12**, 3918 (2025).
- [26] M. D. Jenkins, D. Zueco, O. Roubeau, G. Aromí, J. Majer, and F. Luis, *Dalton Trans.* **45**, 16682 (2016).
- [27] A. Chiesa, S. Roca, S. Chicco, M. de Ory, A. Gómez-León, A. Gomez, D. Zueco, F. Luis, and S. Carretta, *Phys. Rev. Appl.* **19**, 064060 (2023).
- [28] M. Rubín-Osanz, M. C. de Ory, I. Gimeno, D. Granados, D. Zueco, A. Gomez, and F. Luis, *Low Temperature Physics* **50**, 472 (2024).
- [29] O. Noroozian, P. K. Day, B. H. Eom, H. G. Leduc, and J. Zmuidzinas, *IEEE Transactions on Microwave Theory and Techniques* **60**, 1235 (2012).
- [30] P. Pakulski, M. Magott, S. Chorazy, M. Sarewicz, M. Srebro-Hooper, D. Tabor, L. Lapok, D. Szczepanik, S. Demir, and D. Pinkowicz, *Chem* **10**, 971 (2024).
- [31] D. Schäfter, J. Wischnat, L. Tesi, J. A. De Sousa, E. Little, J. McGuire, M. Mas-Torrent, C. Rovira, J. Veciana, F. Tuna, N. Crivillers, and J. van Slageren, *Advanced Materials* **35**, 2302114 (2023).
- [32] O. Armet, J. Veciana, C. Rovira, J. Riera, J. Castaner, E. Molins, J. Rius, C. Miravittles, S. Olivella, and J. Brichteus, *The Journal of Physical Chemistry* **91**, 5608 (1987).
- [33] I. Gimeno, V. Rollano, D. Zueco, Y. Duan, M. C. de Ory, A. Gomez, A. Gaita-Ariño, C. Sánchez-Azqueta, T. Astner, D. Granados, S. Hill, J. Majer, E. Coronado, and F. Luis, *Phys. Rev. Appl.* **20**, 044070 (2023).
- [34] S. Roca-Jerat, M. Rubín-Osanz, M. D. Jenkins, A. Camón, P. J. Alonso, D. Zueco, and F. Luis, *Communications Materials* **6**, 172 (2025).
- [35] M. Mariantoni, F. Deppe, A. Marx, R. Gross, F. K. Wilhelm, and E. Solano, *Phys. Rev. B* **78**, 104508 (2008).
- [36] M. Rubín-Osanz, M. C. de Ory, I. Gimeno, W. Kersten, M. Mas-Torrent, M. C. Pallarés, S. Roca-Jerat, D. Rodriguez, N. González-Prato, J. A. de Sousa, L. Tesi, D. Granados, J. Veciana, D. Zueco, A. Lostao, J. Schmiedmayer, I. Ratera, J. van Slageren, N. Crivillers, A. Gomez, and F. Luis, “Optimizing magnetic coupling in lumped element superconducting resonators for molecular spin qubits,” (2025), arXiv:2511.00857 [quant-ph].
- [37] N. T. Bronn, Y. Liu, J. B. Hertzberg, A. D. Córcoles, A. A. Houck, J. M. Gambetta, and J. M. Chow, *Applied Physics Letters* **107**, 172601 (2015).
- [38] E. Jaynes and F. Cummings, *Proceedings of the IEEE* **51**, 89 (1963).
- [39] G. Vidal and R. F. Werner, *Phys. Rev. A* **65**, 032314 (2002).
- [40] J. R. Schrieffer and P. A. Wolff, *Phys. Rev.* **149**, 491 (1966).
- [41] C. Gardiner and P. Zoller, *Quantum noise: a handbook of Markovian and non-Markovian quantum stochastic methods with applications to quantum optics* (Springer Science & Business Media, 2004).
- [42] T. Holstein and H. Primakoff, *Phys. Rev.* **58**, 1098 (1940).